Sedimentary Geology 454 (2023) 106462

Contents lists available at ScienceDirect

Sedimentary Geology

journal homepage: www.elsevier.com/locate/sedgeo

Decoupled local climate and chemical weathering intensity of fine-grained siliciclastic sediments from a paleo-megalake: An example from the Qaidam basin, northern Tibetan Plateau

Ling Wang [a], Xing Jian [a,*], Hanjing Fu [a], Wei Zhang [a], Fei Shang [b], Ling Fu [b]

[a] State Key Laboratory of Marine Environmental Science, College of Ocean and Earth Sciences, Xiamen University, Xiamen 361102, PR China
[b] Research Institute of Petroleum Exploration and Development (RIPED), PetroChina, Beijing 100083, PR China

ARTICLE INFO

Article history:
Received 12 April 2023
Received in revised form 29 June 2023
Accepted 30 June 2023
Available online 7 July 2023

Editor: Dr. Catherine Chagué

Keywords:
Clay minerals
Geochemistry
Paleo-climate
Megalake
Qaidam basin

ABSTRACT

Clay mineralogy and elemental geochemistry of lacustrine sedimentary records have been widely used in paleo-weathering and paleo-climate studies. However, different paleo-climatic interpretations may be produced via analyses on siliciclastic sediments and other sedimentary components (e.g., authigenic minerals and organic materials), especially for megalake systems. To test this hypothesis, we focus on late Cenozoic lacustrine fine-grained deposits from the northwestern Qaidam basin and combine clay mineralogical and geochemical data (including neodymium isotope) to interpret sediment provenance, reconstruct paleo-weathering history and characterize sediment-climate feedback processes. Provenance analysis results show that the lacustrine siliciclastic sediments were derived from lithologically similar sources that provided dominant felsic parent-rocks. The kaolinite/illite ratio, illite chemistry index, Chemical Index of Alteration (CIA) values are low and demonstrate overwhelmingly mild-moderate chemical weathering intensity, seemingly matching well with the middle–late Miocene regional arid climate. However, these weathering intensity index values are also highly fluctuant and display increasing trends during ~13.4–12 Ma and ~8.8–8.4 Ma. The reconstructed paleo-weathering history is discrepant with local intensified aridity conditions documented by previously published sedimentary carbonate oxygen isotope, evaporite mineral, biomarker and sporopollen data. Given the occurrence of a middle–late Miocene megalake in the Qaidam basin, the intense exhumation at ~13–12 Ma and the ~9 to ~7 Ma intensified East Asian summer monsoon precipitation in northeastern Tibet regions, we suggest that the lacustrine fine-grained siliciclastic compositions and corresponding weathering records were likely influenced by tectonic and climatic changes in far regions to the east. The observed clay mineralogical and geochemical variations reflect weathering conditions involving sediment sources and transport pathways, not merely the depositional areas. Our findings verify the possible differences in paleo-climate reconstruction results from different lacustrine sediment indicators. This study emphasizes the importance of a sediment source-to-sink perspective for paleo-climate study based on siliciclastic materials in megalake systems.

1. Introduction

Clay minerals are commonly regarded as important products of silicate chemical weathering on the Earth's surface (Mei et al., 2021). As chemical weathering processes and intensities are closely linked to climatic conditions, clay mineral-related proxies of weathered rocks, soils, sediments and sedimentary rocks have been widely used to reconstruct paleo-climatic and paleo-environmental history (e.g., Chamley, 1989; Thiry, 2000; Wang et al., 2020; Fu et al., 2022). For example, clay mineral assemblages and ratios (e.g., kaolinite proportion and kaolinite/(kaolinite + chlorite) ratio) have been proposed to indicate regional temperature and precipitation changes and chemical weathering intensity in areas where weathering products are formed (Dinis et al., 2017, 2020; Tateo, 2020). The illite chemistry index is also frequently employed to indicate weathering degrees (Ehrmann et al., 2005; Li et al., 2018; Wang et al., 2020). Since clay minerals are dominant components of fine-grained siliciclastic fractions in sediments (Warr, 2022), geochemical compositions of fine-grained siliciclastic sedimentary rocks are also considered as robust indicators for reconstructing local or regional paleo-weathering and paleo-climate history (Singer, 1984; Li et al., 2018; Bao et al., 2019; Yang et al., 2019). Furthermore, authigenic minerals (e.g., evaporite minerals), organic markers, magnetic susceptibility and some isotopic tracers

* Corresponding author.
E-mail address: xjian@xmu.edu.cn (X. Jian).

https://doi.org/10.1016/j.sedgeo.2023.106462
0037-0738/

(e.g., sedimentary carbonate carbon and oxygen isotopes) of sedimentary records are also useful proxies for paleo-climate reconstruction (Jian et al., 2014; Song et al., 2014; Nie et al., 2017; Liang et al., 2021).

Numerous case studies show that paleo-climate records obtained from detrital clay mineralogical and geochemical compositions of fine-grained siliciclastic sediments correspond well with those based on other proxies in terrestrial and marine deposits (e.g., Zhang et al., 2015, 2016; Yang et al., 2019; Wang et al., 2020). However, it is also realized that fine-grained siliciclastic fractions in sediments may be controlled by climate, weathering and many other processes (e.g., erosion, transport and hydrodynamic sorting) before final deposition in sedimentary basins. Therefore, the fine-grained siliciclastic fractions not only document climate-weathering information of depositional areas, but also reflect other factors in the sediment source-to-sink systems, e.g., parent-rock lithology, topography, transport pathways, post-depositional weathering and even diagenesis (Singer, 1984; Chamley, 1989; Velde, 1992; Fagel, 2007). In this case, such clay mineralogical and geochemical records based on fine-grained siliciclastic sedimentary rocks in complex sedimentary systems, e.g., megalake or marine environments, may produce paleo-climate interpretations concerning a larger and more complicated geographic space, which might be different from those in-situ or biologically related sedimentary indicators in depositional areas, especially for those regions with highly heterogeneous climate conditions.

To test this hypothesis, we focus on the late Cenozoic paleo-weathering and paleo-climate sedimentary record from the northwestern Qaidam basin, northern Tibetan Plateau. The Qaidam basin is an ideal research area due to the continuous Cenozoic fluvial and lacustrine sedimentary sequences and the critical location affected by both the Westerlies and the Asian monsoons (Fig. 1A) (Fang et al., 2007; Song et al., 2014). Numerous studies suggest that a relatively unified megalake existed in the Qaidam basin during the Oligocene–Pliocene (Guo et al., 2018; Liang et al., 2021; Wu et al., 2021; Yu et al., 2021). It is well accepted that the northern Tibetan Plateau has experienced intensified tectonic deformation and crustal shortening since the late Cenozoic (Sun et al., 2005; Zhang et al., 2012; Yuan et al., 2013). Comparatively wet climate in the mid-Miocene Climatic Optimum (MMCO) and subsequently intensified aridification in this region have been revealed and supported by published sporopollen (Miao et al., 2011, 2013), geochemistry (Bao et al., 2019), clay mineralogy (Wang et al., 2013a) and magnetic mineralogy data (Guan et al., 2019; Nie et al., 2019).

In this study, we present clay mineralogical, major-, trace- and rare earth element geochemical and Nd isotopic data from the late Cenozoic subsurface lacustrine deposits in the Xiaoliangshan area (Fig. 1), northwestern Qaidam basin. The aims are to (1) determine sediment provenance and paleo-weathering history of the lacustrine siliciclastic sequences, to (2) discuss the relationship between regional paleo-climate and clay mineralogical and geochemical records and to (3) explore potential controls on fine-grained siliciclastic compositions in a paleo-megalake system.

2. Geological setting

2.1. Geology of the Qaidam basin and the surrounding mountains

The Qaidam basin is the largest Cenozoic sedimentary basin in northern Tibet (Fig. 1), covering approximately an area of 120,000 km^2. The elevations of the Qaidam basin vary from 2.7 to 3 km. The basin is surrounded by the Eastern Kunlun Mountains, Qilian Mountains and Altyn Tagh Mountains to the south, northeast and northwest, respectively (Fig. 1B). These mountains are in average >5 km above sea level. The Eastern Kunlun Mountains are regarded as a ~1000 km-long, latitudinally trending, granitoid-rich orogenic belt and mainly consist of igneous rocks (especially granitoid rocks of arc origin) with subordinate metamorphic rocks, sedimentary rocks and ophiolite-related rocks (Yuan et al., 2003; Mao et al., 2014; C. Wu et al., 2019). The Eastern Kunlun orogenic belt is believed to document subduction-closure of the Proto-Tethys and Paleo-Tethys Oceans during the Paleozoic to early Mesozoic (Jian et al., 2023). The Qilian Mountains, as a ~300 km-wide, ~1000 km-long, metamorphic rock-rich fold-thrust belt, are mainly composed of different grades of metamorphic rocks (e.g., schist, gneiss and marble), plutonic rocks, marine sedimentary rocks as well as ophiolite-related rocks (Gehrels et al., 2003; Xiao et al., 2009; S. Song et al., 2013). The Qilian Mountains developed in response to multiple subduction- and collision-related processes during the closure of the Proto-Tethys Ocean (Xiao et al., 2009; Jian et al., 2023). The Altyn Tagh Mountains separate the Qaidam basin from the Tarim basin and are featured by an active left-lateral strike-slip fault (i.e., the Altyn Tagh Fault) with ~375 km offset (Shen et al., 2001; Yin et al., 2002). The Altyn Tagh Mountains are mainly composed of marine sedimentary and metamorphic rocks (such as gneiss, marble and amphibolite), with minor igneous rocks, similar to the rock assemblages in the Qilian Mountains (Zhang et al., 2001; Gehrels et al., 2003).

Formation of the Cenozoic Qaidam basin is regarded as a result of a convergence system on the northern margin of the Tibetan Plateau (Tapponnier et al., 2001). The tectonic regime of the basin has been closely related to the Indo-Asian collision and the subsequent continuous rise, thickening, shortening and lateral compression in the Tibetan Plateau (Tapponnier et al., 2001; Yin et al., 2002, 2008; Zhuang et al., 2011b; Jian et al., 2018). A series of thrust fold belts with NW-SE direction are developed along the basin margin and within the basin (Fig. 1C).

The Qaidam basin preserves continuous and thick Cenozoic fluvial-lacustrine sedimentary successions, up to 12 km in thickness (Fang et al., 2007; Meng and Fang, 2008; Yin et al., 2008; Jian et al., 2014; Bush et al., 2016; Bao et al., 2017). The Cenozoic sedimentary strata of the Qaidam basin are generally divided into 7 stratigraphic units (Fig. 2), including Lulehe Formation (E_{1+2}), Xiaganchaigou Formation (E_3), Shangganchaigou Formation (N_1), Xiayoushashan Formation (N_2^1), Shangyoushashan Formation (N_2^2), Shizigou Formation (N_2^3), and Qigequan Formation (Q_{1+2}), ages of which were constrained by magnetostratigraphic investigations combined with paleontological data (e.g., Sun et al., 2005; Zhang, 2006; Fang et al., 2007; Lu and Xiong, 2009; Song et al., 2014; Chang et al., 2015; Ji et al., 2017; T. Zhang et al., 2018). The Cenozoic strata show highly spatial and stratigraphic variations in lithology (Fig. 2). The southwestern and northwestern Qaidam basin are characterized by mixed carbonate-siliciclastic deposits with evaporite layers (Fig. 2) (Jian et al., 2014; Chang et al., 2015), while the northern and northeastern Qaidam basin are dominated by siliciclastic deposits (Fig. 2) (Cheng et al., 2021; Fu et al., 2022). Generally, the Cenozoic strata of the Qaidam basin display a stacking pattern of coarse-grained deposits in the bottom (E_{1+2}), followed by dominant fine-grained deposits (E_3, N_1 and N_2^1) and then coarse-grained deposits in the upper part (N_2^2, N_2^3 and Q_{1+2}) for most regions (Guan and Jian, 2013; Zhuang et al., 2011b).

2.2. Depositional ages of the western Qaidam basin

Several magnetostratigraphy studies on Cenozoic sedimentary outcrop and borehole sections from the western Qaidam basin have recently been completed (Zhang, 2006; Zhang et al., 2013; Song et al., 2014; Chang et al., 2015; T. Zhang et al., 2018). The N_1, N_2^1, N_2^2, and N_2^3 strata from the Xichagou section (see Fig. 1B for location) were dated at 31–22 Ma, 22–14.9 Ma, 14.9–8.2 Ma, and <8.2 Ma, respectively, according to investigations by Zhang (2006). The Huatugou section (see Fig. 1B for location) spans a period from ~30 Ma to ~11 Ma and comprises the N_1 strata (>31–~23 Ma), N_2^1 strata (~23–12.44 Ma), and N_2^2 strata (<12.44 Ma) (Chang et al., 2015). In this study, the Xiaoliangshan area stratigraphy was correlated with the Honggouzi (HGZ) section (see Fig. 1B for location) near the Xiaoliangshan area. The depositional ages of N_2^2 and N_2^3 strata of the HGZ section were

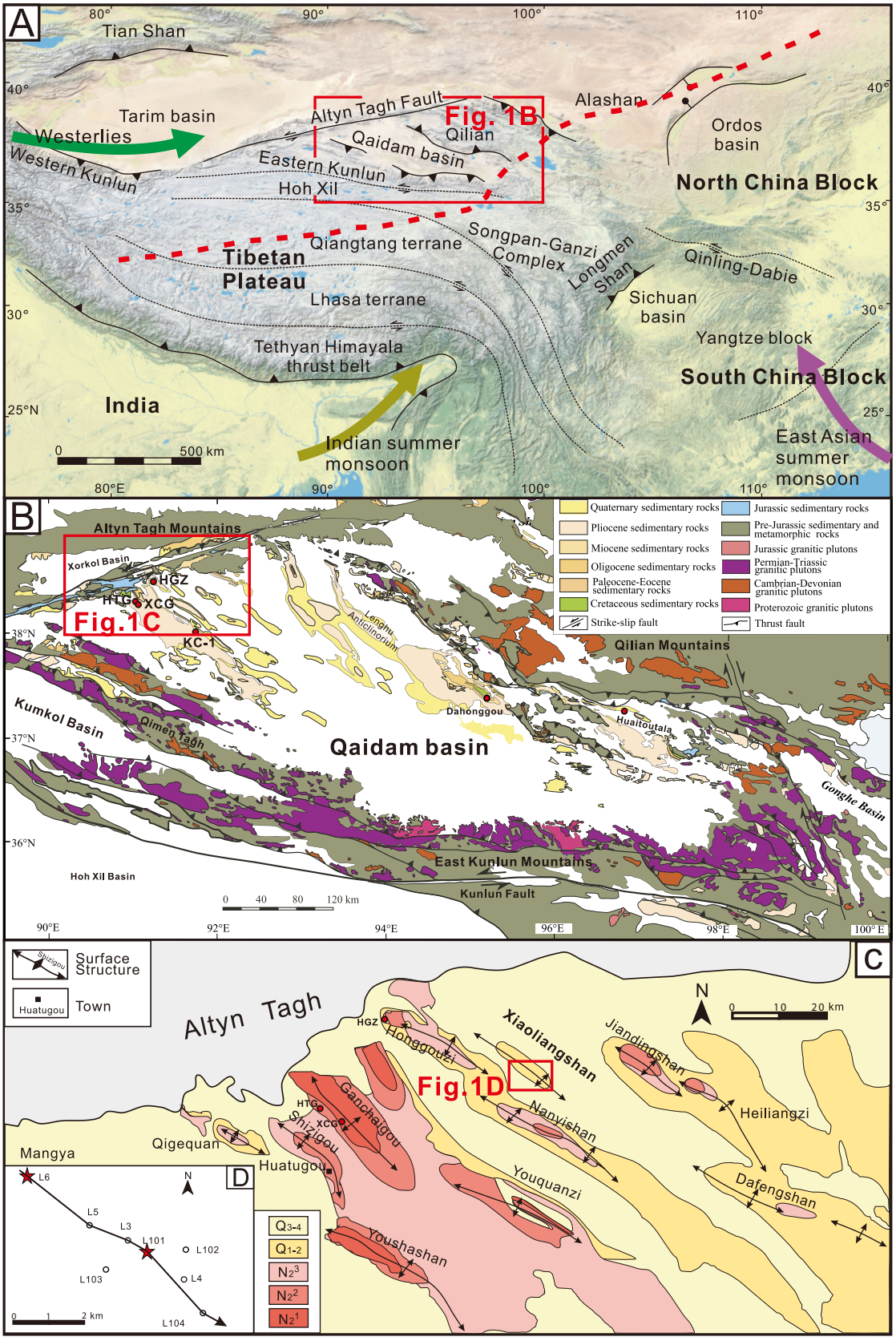

Fig. 1. Geological setting and local maps of the study area. (A) A map showing major tectonic elements in the Tibetan Plateau and the surrounding regions, modified from Jian et al. (2020a). The red dashed line represents the current boundary of the Asian summer monsoon and Westerlies belts, after Nie et al. (2017). (B) The geological map of the Qaidam basin and surrounding mountains, revised from Lu et al. (2018). (C) The geological map of the Xiaoliangshan area and the northwestern Qaidam basin, revised from W. Zhang et al. (2018). (D) Major hydrocarbon exploration well locations in the Xiaoliangshan area. HGZ: Honggouzi section; HTG: Huatugou section; XCG: Xichagou section; N_2^1: Xiayoushashan Formation; N_2^2: Shangyoushashan Formation; N_2^3: Shizigou Formation; Q_{1-2}: Qigequan Formation; Q_{3-4}: Holocene.

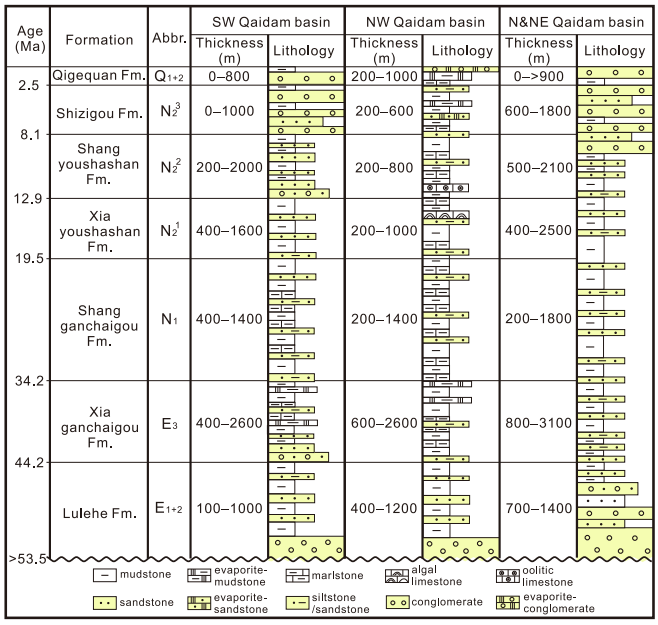

Fig. 2. Cenozoic stratigraphy and lithology of the Qaidam basin, compiled from Fang et al. (2007), Meng and Fang (2008), Zhuang et al., 2011b, Jian et al. (2013), Ji et al. (2017) and Cheng et al. (2021). Note that the depositional ages of the stratigraphic units are from Ji et al. (2017).

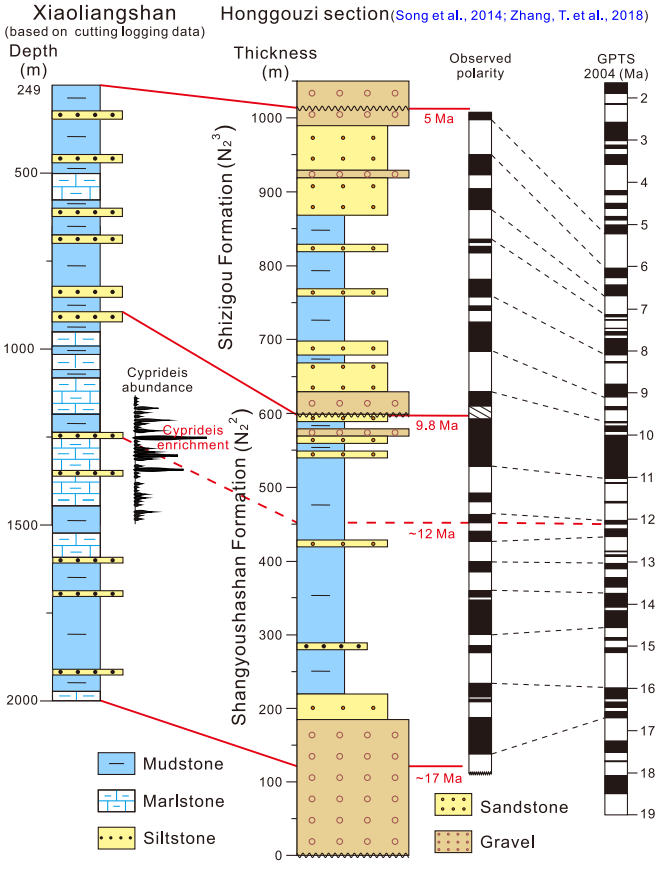

Fig. 3. Stratigraphic correlation between the Xiaoliangshan area (this study) and the Honggouzi section (Song et al., 2014; T. Zhang et al., 2018), western Qaidam basin. Since the rock cores were not continuously collected, the lithology column of the Xiaoliangshan here was based on cutting logging data from Wang et al. (2012).

restricted as ~17 Ma to 9.8 Ma and 9.8 Ma to 5 Ma by a comprehensive magnetostratigraphic investigation combined with paleontological data (Song et al., 2014; T. Zhang et al., 2018; Fig. 3). The timing of the Cyprideis enrichment in the Miocene strata of the Xiaoliangshan area is consistent with that of the entire Qaidam basin (~12 Ma; Zhang et al., 2006; Fig. 3), supporting the application of this age model to depositional age estimation of the Miocene strata in this study. Using this age model, we were able to interpolate the absolute age to ~13.4 Ma for the lowermost Well L101 sample and to 8.4 Ma for the uppermost sample. The stratigraphic correlation between Wells L101 and L6 is shown in Fig. S1 in Appendix B.

2.3. Miocene sedimentary environments in the Xiaoliangshan area

The Miocene strata in the Xiaoliangshan area of the Qaidam basin are primarily composed of mixed carbonate-siliciclastic fine-grained rocks (Figs. 4, 5). These sedimentary rocks are thought to be deposited in lake environments (from a semi-deep fresh-water to semi-brackish-water lake environment to a shallow brackish-water lake environment) under a relatively arid climate (Fig. 4) (Jian et al., 2014; W. Zhang et al., 2018). The paleo-lake in this region is considered to be hydrologically closed with intermittently open conditions (Jian et al., 2014). Deposits spanning this interval consist of three main lithofacies: Facies 1 is interpreted as deposited in a semi-deep fresh-water to semi-brackish-water lake environment by a combination of gray-black mudstone and marlstone with well-developed horizontal millimeter-scale-laminations and the occurrence of pyrite nodules; Facies 2 is characterized by gray, yellowish massive mudstone, marlstone and siltstone with absent laminations, centimeter-sized anhydrite and gypsum crystals, indicating a shallow brackish-water lake environment; Facies 3 is mainly composed of yellowish massive sandstone with abundant anhydrite and gypsum crystals, also deposited in a shallow brackish-water lake environment (Jian et al., 2014). Facies 1 is predominantly present in the N_2^2 strata. Facies 2 and Facies 3 mainly occur in the N_2^3 strata (Jian et al., 2014; Figs. 4, 5). More detailed facies descriptions and representative photographs are shown by Jian et al. (2014). Abundant hydrocarbon resources are trapped in these shallow (most <2000 m) subsurface N_2^2 and N_2^3 sedimentary strata (W. Zhang et al., 2018) and several exploration wells were drilled in the Xiaoliangshan area (Fig. 1D) (Jian et al., 2014). The analyzed samples in this study were collected from Wells L101 and L6 and were from the upper part of the N_2^2 strata and the lower N_2^3 strata (Fig. 1; Fig. S1 in Appendix B).

3. Materials and methods

3.1. Sample analysis

A total of 48 samples were selected for clay mineralogical analysis. Samples were crushed, placed into 100 mL centrifuge tube and immersed in pure water for 30 min. After oscillation and stirring, 0.05 mg sodium hexametaphosphate was added to prevent clay flocculation. The clay fractions (<2 μm) were then separated by gravitational sedimentation following the Stokes' law. Organic matter and carbonate were removed by 10 % H_2O_2 and 1 mol/L CH_3COOH, respectively. To identify and quantify the clay mineral compositions, each sample was suspended (dispersed by ultrasonic treatment), pipetted and deposited onto a glass slide and allowed to air-dry at room temperature. The clay mineral compositions of these oriented samples were then determined by a Rigaku Ultima IV X-ray diffractometer (XRD) in the following conditions: air-dried (N), ethylene glycol-solvated (EG) and heated to 500 °C for 2 h (T). All samples were scanned from 4° to 35° with a scanning speed of 4°/min under 40 kV, 30 mA, wavelength of 1.5406 and step width of 0.02° conditions.

We selected 29 fine-grained sediment samples for major-, trace- and rare earth element geochemistry analysis and 10 fine-grained sediment samples for Nd isotope analysis. All the samples were powdered and

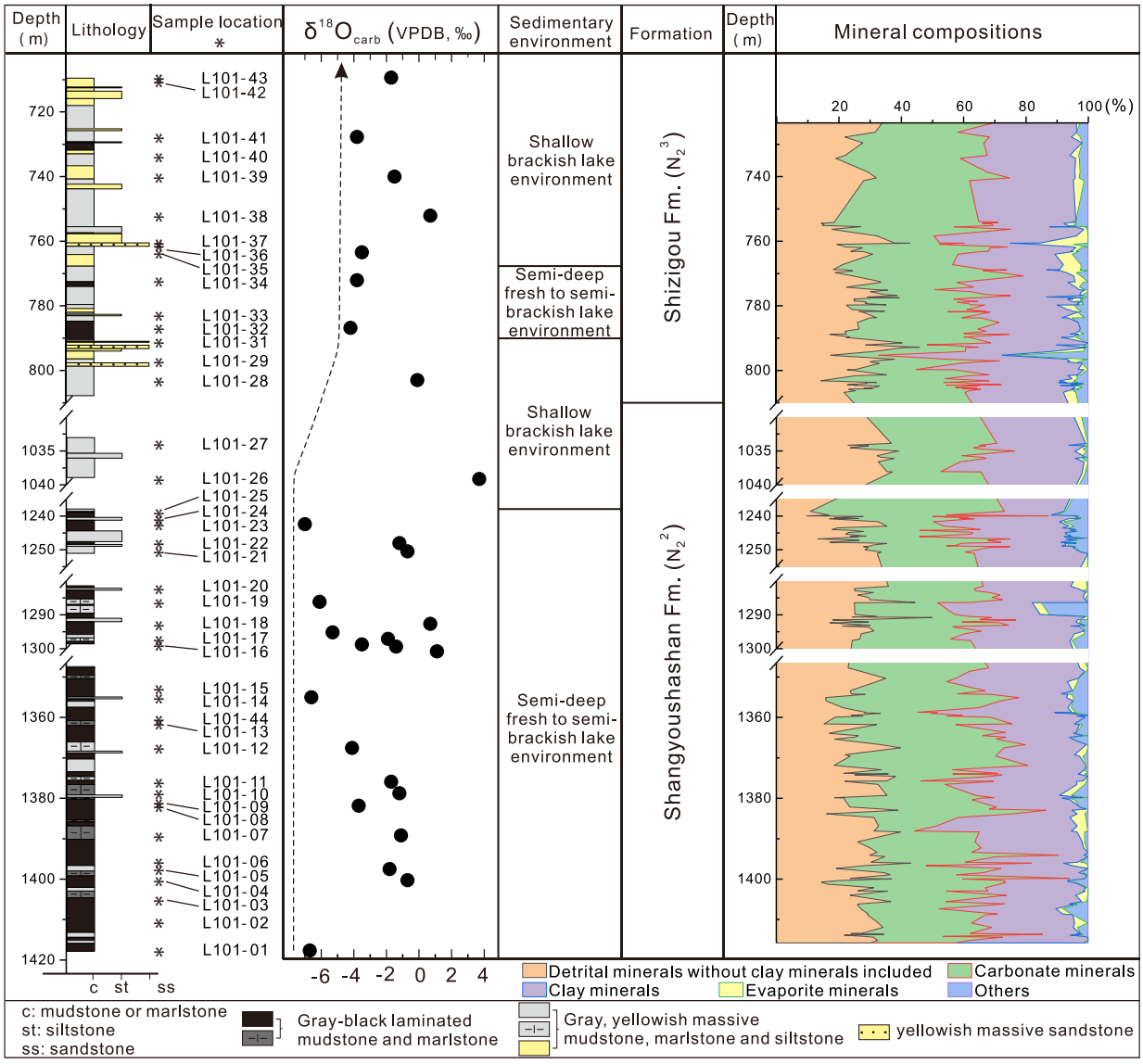

Fig. 4. Lithological column, sedimentary carbonate $\delta^{18}O$ ($\delta^{18}_{carb}O$) values, sedimentary environment interpretation (Jian et al., 2014) and whole-rock mineral compositions (W. Zhang et al., 2018) of rock cores from the Well L101 in the Xiaoliangshan area. The high oscillations in $\delta^{18}_{carb}O$ data are thought to be dependent on variable precipitation/evaporation ratios, specifically the residence time of lake water and corresponding calcite proportions in carbonate fractions (Jian et al., 2014). Samples with the highest calcite contents (100 % or nearly 100 %, in carbonates) indicate the most negative $\delta^{18}_{carb}O$ values (arrow mark), implying hydrologically open lake conditions with minimal evaporation. Detrital minerals include quartz, K-feldspar and plagioclase. Carbonate minerals include calcite, dolomite, aragonite, siderite and magnesite. Evaporite minerals include gypsum, anhydrite and halite. Others include hematite and pyrite. Refer to Jian et al. (2014) and W. Zhang et al. (2018) for the details.

treated with 10 % H_2O_2 and 5 mol/L CH_3COOH under 60 °C water bath conditions to remove organic matter and carbonate and then the siliciclastic residues were separated and dried.

Major elements were measured by an X-ray fluorescence (XRF) spectrometer following the procedures described by Mei et al. (2021). The sample powders were dried at 105 °C, accurately weighed and placed into Pt—Au crucibles, and then fully mixed with lithium metaborate flux. The mixed materials were melted at 1050 °C and were then cooled to form melting disks for XRF analysis. The loss on ignition (LOI) values were obtained by measuring the mass reduction after heating the samples at 1000 °C. The accuracy (relative deviation) for the determination of major element concentrations is <5 %.

Trace- and rare earth elements were measured by an Inductively Coupled Plasma Mass Spectrometer (ICP-MS) following the procedures described by Mei et al. (2021). The sample powders were accurately weighed, placed in high-pressure-resistant Teflon beakers and completely digested with HNO_3 and HF mixtures. The BHVO-2, AGV-2 and W-2 standard materials were used to monitor the analytical quality. All the relative deviations between measured and certified values are generally <5 %.

The Nd isotopic analysis was performed following the procedures described by Jian et al. (2020b). The pre-treated samples (~50 mg) were weighed accurately and reacted with a mixture of concentrated HF and HNO_3 for 48 h in a high-pressure muff furnace at 190 °C. Element Nd was then separated following standard ion exchange techniques and Nd isotopes were measured using a Multi-Collector Inductively Coupled Plasma Mass Spectrometer (MC-ICP-MS). The GBS 04-3258-2015 ($^{143}Nd/^{144}Nd = 0.512438 \pm 10$, 2σ, J. Li et al., 2017) standard solution was applied to monitor the quality of Nd isotopic measurements and gave an average value of measured $^{143}Nd/^{144}Nd = 0.512438 \pm 10$ (2σ, $N = 7$), well within the recommended value ranges.

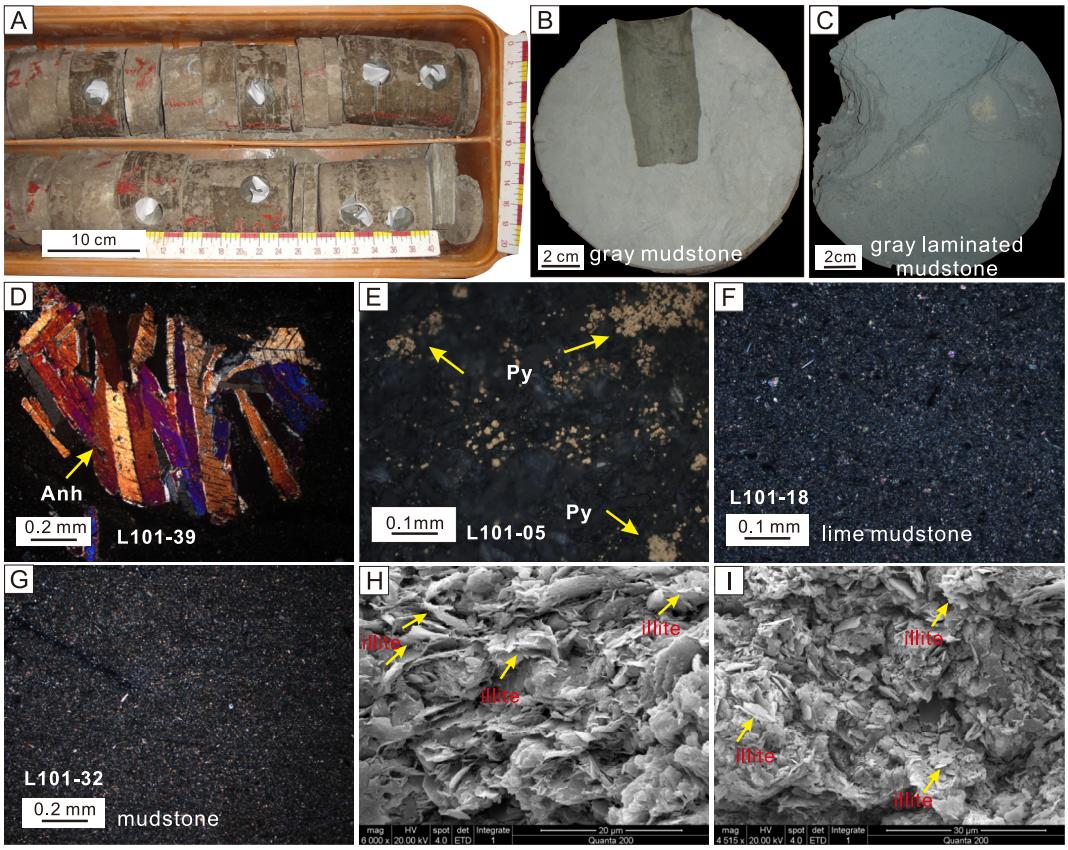

Fig. 5. Representative photographs, microphotographs (under the cross-polarized light) and the scanning electron microscope (SEM) pictures for the samples from Well L101. (A) macroscopic view of laminated mudstone (1410 m–1412 m); (B) gray mudstone (1403.8 m); (C) gray laminated mudstone (1242.63 m); (D) anhydrite (Anh) crystals in a mudstone sample (739.8 m); (E) marlstone with authigenic pyrite (Py, reflected light, 1397.5 m); (F) lime marlstone (1292.94 m); (G) mudstone (787.34 m); (H) and (I) SEM pictures of clay minerals at the depth of 769.03 m and 1296.84 m, respectively, from Wang et al. (2012).

3.2. Calculation of clay mineral- and element-based weathering intensity indices

The JADE 6.0 software was used to identify clay minerals from the obtained XRD spectra (Fig. 6). Generally, illite can be recognized by peaks at 10 Å (001), 5 Å (002) and 3.33 Å (003) on the N-treated diffractogram, which show no changes after being treated with ethylene glycol (Fig. 6). The (002) peak (7.1 Å) of chlorite almost coincides with the (001) peak (7.2 Å) of kaolinite on the EG-treated diffractogram (Fig. 6). Kaolinite and chlorite can be distinguished by the (002) peak (3.58 Å) of kaolinite and (004) peak (3.54 Å) of chlorite (Fig. 6). Besides, chlorite was also identified by its (001) peak (14.2 Å) and (003) peak (4.74 Å) on EG-treated diffractogram (Fig. 6). Smectite (including illite/smectite mixed-layers) can be recognized by a combination of the N- and EG-treated diffractograms. The peak of smectite from 12 Å to 15 Å on the N-treated diffractogram will move to 17 Å after being treated with ethylene glycol (Fig. 6). After the identification of each clay mineral, semi-quantitative estimations of the relative percentages of clay minerals were based on the peak area (Biscaye, 1965) on XRD patterns of the EG-treated samples. The relative abundances of clay minerals were determined by the formula: 4×I (illite 10 Å) + I (smectite 17 Å) + 2×I (kaolinite, chlorite 7.1 Å) = 100 % (Biscaye, 1965; Song et al., 2018; Fu et al., 2022). The relative proportions of kaolinite and chlorite (kaolinite/chlorite) were determined based on the ratio of the 3.58/3.54 Å peak areas. The illite chemistry index (illite 5 Å/10 Å), defined as the ratio of the 5 Å and 10 Å peak areas, was also calculated for paleo-weathering intensity evaluation.

Chemical weathering intensity can also be quantified by several proxies based on chemical elemental mobility (Nesbitt and Young, 1982; Fedo et al., 1995; Yang et al., 2019; Mei et al., 2021), such as the Chemical Index of Alteration (CIA = [Al_2O_3 / (Al_2O_3 + CaO* + Na_2O + K_2O)] × 100, in molecular proportions; Nesbitt and Young, 1982). CaO* therein represents CaO content in the silicate fraction. Although we attempted to remove CaO in the carbonate fraction through acid digestion, we found that the carbonate minerals in some samples might not be completely removed (Table S2 in Appendix A; the duration of complete carbonate removal is various depending on several factors (Fu et al., 2020)). Hence, we accepted a widely-used method proposed by McLennan (1993) that if the molar content of CaO was no more than that of Na_2O in the sample, we adopted the molar content of CaO as CaO* value. Conversely, if the CaO molar content was more than the Na_2O molar content, we assumed that the CaO* value was equal to the Na_2O molar content (Bock et al., 1998; Roddaz et al., 2006).

Grain size and mineral sorting may affect sediment chemical compositions and thus bias the CIA indication of chemical weathering intensity (Bouchez et al., 2011; Ren et al., 2019). Hence, it is necessary to consider and eliminate the potential grain-size effect on the CIA proxy. We note the remarkably positive correlation between raw CIA values and Al/Si molar ratios (a reliable indicator of sediment grain size; Lupker et al., 2013; Li et al., 2022) (Fig. S2 in Appendix B), suggesting non-negligible grain-size dependence. Here, we normalized the raw CIA data to a uniform grain size, following the method proposed by Li et al. (2022). The corrected CIA (CIA_C) can be expressed as follows:

$$CIA_C = CIA_r - \left[(Al/Si)_S - (Al/Si)_N\right] \times S \quad (1)$$

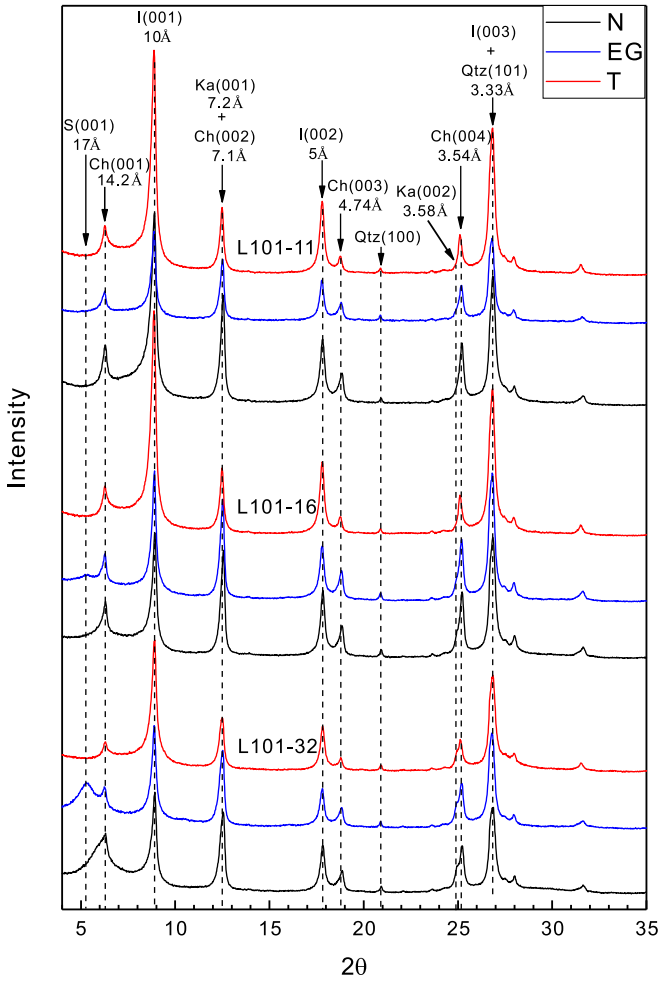

Fig. 6. Clay X-ray diffraction patterns of three representative samples from Well L101. S: Smectite; Ch: Chlorite; Ka: Kaolinite; I: Illite; Qtz: Quartz; N: air-dried; EG: ethylene-glycol solvation; T: heated to 500 °C for 2 h.

where CIA_r is the raw CIA value and S is the slope of the fitted linear regression line of the raw CIA values and Al/Si ratios. $(Al/Si)_S$ is the sample Al/Si value and $(Al/Si)_N$ is the uniform value for normalization. As shown in Fig. S2 in Appendix B, the correlation shows a linear correlation ($R^2 = 0.50$), and the slope of 48.33 in this composite line can be used as S for the CIA correction in Eq. (1). We use 0.35 (mean value of Al/Si ratios) as the $(Al/Si)_N$ value in this study. The corrected CIA values have no apparent correlation with the Al/Si molar ratios, implying that this correction can eliminate the grain-size effect (Fig. S2 in Appendix B).

4. Results

4.1. Clay mineral compositions

Representative XRD patterns of the N-, EG-, and T-treated clay mineral samples are illustrated in Fig. 6 and the data are given in Table S1 in Appendix A. The results indicate that the N_2^2 and N_2^3 samples have similar clay mineral assemblages, characterized by abundant illite (70.0 %–91.2 % for N_2^2 and 58.8 %–89.9 % for N_2^3) and chlorite (5.0 %–23.3 % for N_2^2 and 6.9 %–25.2 % for N_2^3), subordinate kaolinite (1.7 %–11.8 % for N_2^2 and 1.0 %–11.6 % for N_2^3) and scarce smectite (0.0 %–2.6 % for N_2^2 and 0.0 %–13.4 % for N_2^3) (Fig. 7). The clay mineral assemblages of N_2^2 samples have almost unchanged trends of average values over time but show large fluctuations in individual values. The N_2^3 samples are also highly fluctuant in clay mineral assemblages. However, the chlorite and kaolinite contents in the N_2^3 samples are featured by decreasing trends during ~9.2–8.8 Ma and then increasing trends during ~8.8–8.4 Ma (Fig. 7). Illite contents show the contrary trends. Moreover, the kaolinite/illite (Ka/I) values remain stable during ~13.4–12 Ma in N_2^2 samples, while the N_2^3 samples show a slightly decreasing trend during ~9.2–8.8 Ma and then a slightly increasing trend during ~8.8–8.4 Ma (Fig. 8A). The illite 5 Å/10 Å values range from 0.13 to 0.42 (avg. = 0.30) for N_2^2 samples and from 0.13 to 0.45 (avg. = 0.32) for N_2^3 samples (Fig. 8B). Slightly different from the Ka/I ratios, the illite 5 Å/10 Å values are obviously fluctuant in N_2^2 samples (Fig. 8B).

4.2. Major-, trace- and rare earth element compositions

The raw major element data are given in Table S2 in Appendix A. Overall, all samples show high abundances of SiO_2 (29.25–67.34 wt.%, avg. = 53.58 wt.%) and Al_2O_3 (9.48–18.80 wt.%, avg. = 15.87 wt.%), and relatively low abundances of CaO (0.76–12.90 wt.%, avg. = 3.18 wt.%), K_2O (2.03–4.14 wt.%, avg. = 3.37 wt.%) and Na_2O (0.94–2.21 wt.%, avg. = 1.72). The element compositions of all the samples are normalized to the composition of the Upper Continental Crust (UCC, Rudnick and Gao, 2003) and are shown in Fig. S3 in Appendix B. The results indicate that most samples are moderately depleted in elements Na and Ca and are slightly enriched or depleted in element K (Fig. S3 in Appendix B). Both the raw CIA (58.6–68.4, avg. = 63.6) and corrected CIA (60.6–66.3, avg. = 63.6) values show increasing trends for the N_2^2 samples during ~13.4 Ma–12 Ma (Fig. 8C, D). Nevertheless, the N_2^3 samples display slight, complicated variations in both raw CIA and corrected CIA values. The raw CIA values decrease from ~9.2 Ma to ~9 Ma and then increase during ~9 Ma–8.4 Ma. The corrected CIA values show a decreasing trend from ~9.2 Ma to ~8.8 Ma and an increasing trend during ~8.8 Ma–8.4 Ma (Fig. 8C, D).

The trace- and rare earth element data are given in Tables S3–S4 in Appendix A and representative elemental ratios are illustrated in Fig. 7. All samples have relatively approximate trace elemental ratios, such as Th/Sc (0.77–1.01) and La/Th (2.08–2.78) (Fig. 7). The UCC-normalized trace element patterns of all the analyzed samples are plotted in Fig. S3 in Appendix B. The rare earth element (REE) concentrations are further normalized to chondritic compositions (Taylor and McLennan, 1985) and the REEs of the Post-Archean Australian Shale (PAAS; McLennan, 1989) and UCC (Rudnick and Gao, 2003) are also plotted for comparison purposes (Fig. 9B). All samples show similar REE patterns to PAAS and UCC, with relatively high abundances of the light rare earth elements (LREE; La_N/Yb_N = 6.38–9.54, avg. = 8.72) and flat patterns for heavy rare earth elements (HREE; Gd_N/Yb_N = 1.26–1.77, avg. = 1.47). In addition, all samples show significantly negative Eu anomalies, normalized to chondritic compositions (Eu/Eu^* = 0.63–0.83, avg. = 0.68; Fig. 9B).

4.3. Nd isotopes

Neodymium isotopic results of the analyzed samples are expressed by $^{143}Nd/^{144}Nd$ ratios and εNd values ($\varepsilon Nd = (((^{143}Nd/^{144}Nd)_{measured} / (^{143}Nd/^{144}Nd)_{CHUR} - 1) \times 10^4$, CHUR = 0.512638 (Jacobsen and Wasserburg, 1980)). The siliciclastic fractions have fairly small range of $^{143}Nd/^{144}Nd$ ratio values from 0.512111 to 0.521145 (avg. = 0.512127) and εNd(0) values from −10.29 to −9.62 (avg. = −9.96) (Table 1; Fig. 7).

5. Discussion

5.1. Sediment clay mineral formation on the Earth's surface and evaluating other processes in addition to weathering

Although clay minerals can be formed through direct precipitation from water body and deep-burial diagenetic transformation (Chamley, 1989; Thiry, 2000; Fagel, 2007), previous studies suggest that clay

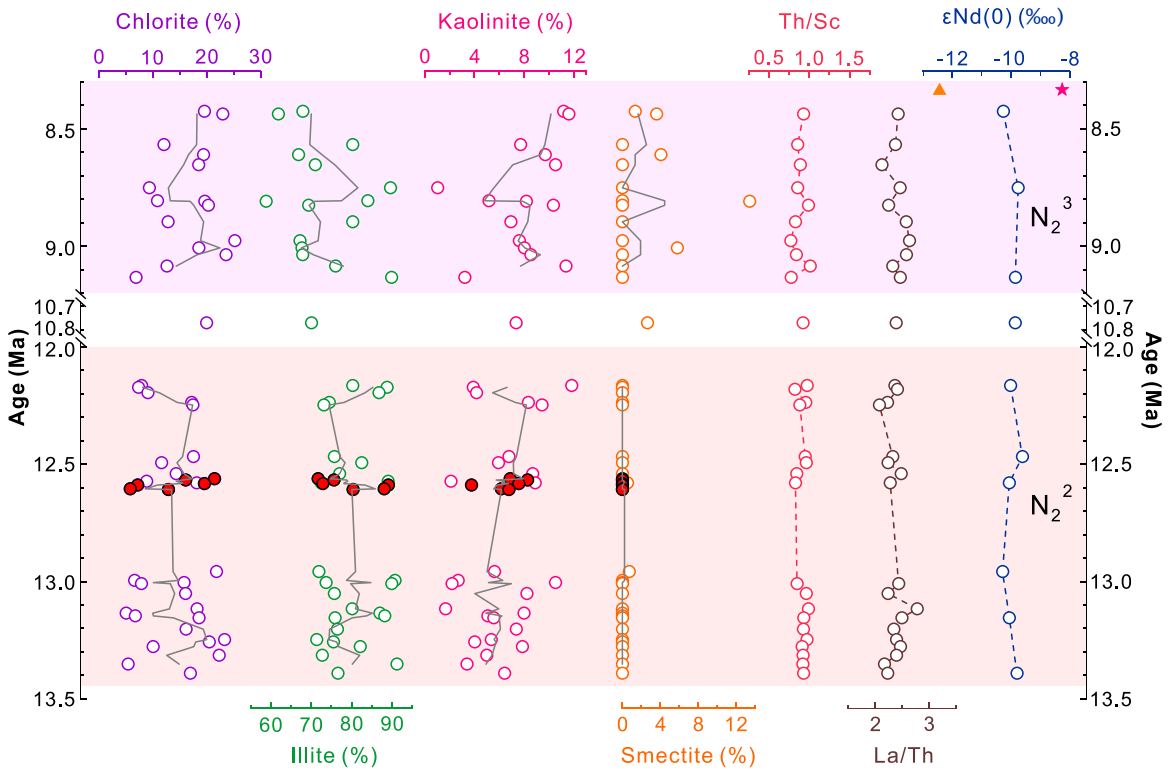

Fig. 7. Vertical variations in relative abundances of clay minerals (chlorite, illite, kaolinite and smectite), Th/Sc ratio, La/Th ratio and εNd(0) values of the analyzed siliciclastic sediment samples from Well L101 and Well L6. Red solid circles represent samples from Well L6. Note that the orange triangle and pink star stand for the mean εNd(0) values of modern fluvial sediments from the Qilian Mountains and Eastern Kunlun-Qaidam terrane (Fig. S5 in Appendix B), respectively (Wu et al., 2010). The gray solid lines represent three-point running average processing results.

minerals in lake, river sediments and sedimentary rocks are most detrital (Yang et al., 2019; Deconinck et al., 2019; Wang et al., 2020). Specifically, kaolinite is generally considered to be formed by decomposition of feldspar, mica and pyroxene under strong leaching and warm-wet climatic conditions (e.g., in warm and humid climatic belt). Chlorite mainly originates from low-grade metamorphic rocks and ferromagnesian rocks suffering slight chemical weathering, while illite is formed by weathering and depotassication of aluminosilicate minerals (such as feldspar and mica) in dry and cold environments (Liu et al., 2007; Wang et al., 2013b; Deconinck et al., 2019). Smectite can be produced

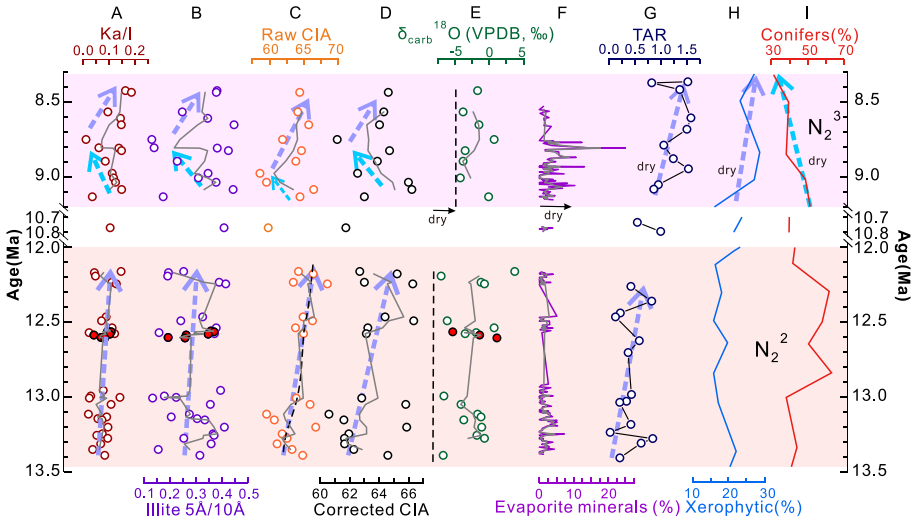

Fig. 8. Temporal variations in paleo-climate proxy values of the analyzed samples from this study and from previous studies. (A) Kaolinite/illite ratio (Ka/I) in the Qaidam basin from Well L101 and Well L6 (this study); (B) illite chemistry index (illite 5 Å/10 Å) in the Qaidam basin from Well L101 and Well L6 (this study); (C) raw CIA in the Qaidam basin from Well L101 (this study); (D) corrected CIA in the Qaidam basin from Well L101 (this study); (E) sedimentary carbonate $\delta^{18}O$ ($\delta^{18}_{carb}O$) values of the Xiaoliangshan area from Well L101 and Well L6 (Jian et al., 2014); (F) evaporite mineral percentage (including gypsum, anhydrite and halite) of the Xiaoliangshan area from Well L101 (W. Zhang et al., 2018); (G) terrigenous/aquatic ratio (TAR = $(C_{27} + C_{29} + C_{31})/(C_{15} + C_{17} + C_{19})$ of the n-alkanes) from the borehole KC-1 (see Fig. 1B for location) (Liang et al., 2021); (H) xerophytic and (I) conifers percentage from the borehole KC-1 (Miao et al., 2013). The gray solid lines represent three-point running average processing results.

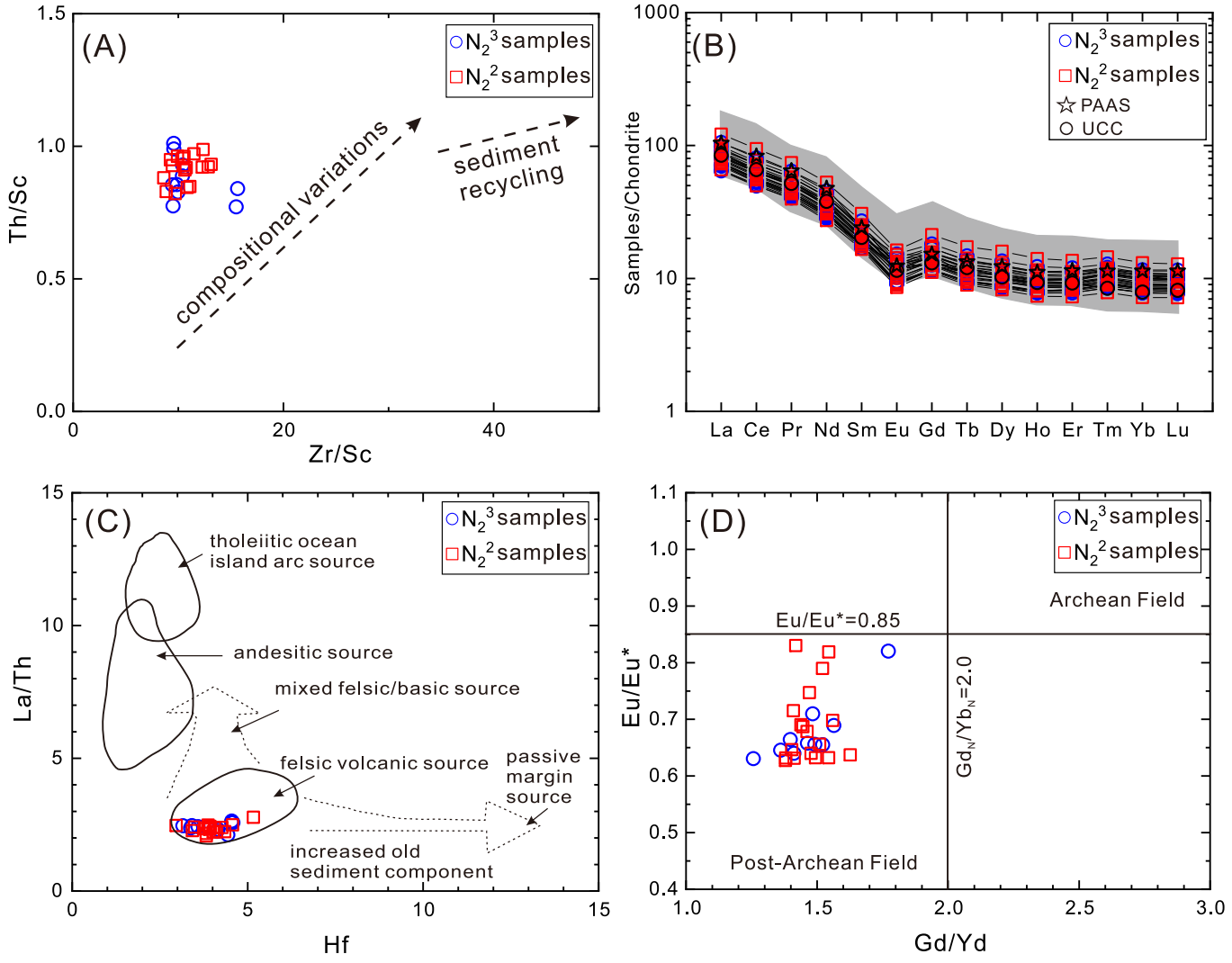

Fig. 9. (A) Th/Sc vs. Zr/Sc binary plots (interpretations after McLennan et al., 1993). (B) REE concentrations normalized by chondrite compositions and compared with UCC and PAAS compositions. The gray band represents compiled data from Jian et al. (2013). (C) La/Th vs. Hf binary plots for the analyzed samples (modified from Floyd and Leveridge, 1987); (D) Eu/Eu* vs. Gd_N/Yb_N binary plots for the analyzed samples (modified from McLennan, 1989). The trace element geochemical results show that the sediments have a predominant felsic source composition.

under alternate wet and dry conditions, through moderate chemical weathering in poor drainage basin environments (Chamley, 1989; Liu et al., 2007).

Before examining the paleo-climatic and paleo-environmental significance of clay minerals, it is quite important to confirm that they are dominantly detrital in origin without significant influence of burial diagenesis (Deconinck et al., 2019). Diagenetic transformation processes of clay minerals generally occur at a temperature of 100–140 °C (Chamley, 1989; Song et al., 2018). Previous studies suggest that the average geothermal gradient of end-Oligocene–end-Miocene strata in the

Table 1
Nd isotopic data and source modeling results of the analyzed sediment samples.

Sample name	$^{143}Nd/^{144}Nd$	2σ	$\varepsilon_{Nd}(0)$ (‰)	Modeling results
L101–43	0.512112	0.000004	−10.27	0.47QL + 0.53EKQ
L101–38	0.512137	0.000004	−9.77	0.35QL + 0.65EKQ
L101–28	0.512133	0.000006	−9.86	0.37 QL + 0.63EKQ
L101–27	0.512132	0.000004	−9.87	0.37 QL + 0.63EKQ
L101–26	0.512124	0.000004	−10.02	0.41 QL + 0.59EKQ
L101–20	0.512145	0.000004	−9.62	0.31 QL + 0.69EKQ
L101–16	0.512122	0.000004	−10.07	0.42 QL + 0.58EKQ
L101–15	0.512111	0.000006	−10.29	0.47 QL + 0.53EKQ
L101–08	0.512122	0.000004	−10.07	0.42 QL + 0.58EKQ
L101–01	0.512136	0.000004	−9.80	0.36 QL + 0.64EKQ
Qilian (QL)[a]	0.511998		−12.49	
Eastern Kunlun-Qaidam (EKQ)[a]	0.512231		−8.30	

[a] Nd isotopic data of the QL and EKQ are from Wu et al. (2010).

western Qaidam basin is 32.6–31.0 °C/km (Qiu, 2002), which means that the maximum temperature corresponding to our sampling depth (<1700 m) might not be enough to prompt diagenetic transformation. Besides, the N_2^2 and N_2^3 strata of Well L101 have low vitrinite reflectance (Ro) values, ranging from 0.53 % to 0.7 % and <0.53 %, respectively (Wang et al., 2012). The low values of pyrolysis temperature (T_{max}) (406–419 °C for N_2^2 strata and 365–409 °C for N_2^3 strata) measured from Well L101 indicate that the organic matter is immature (Wang et al., 2012). These data confirm a weak influence of thermal diagenesis linked to burial (Dellisanti et al., 2010). In addition, the clay mineral assemblages do not systematically change with depth throughout the core (Fig. 7). Therefore, we suggest that the burial diagenesis had little influence on the clay mineral assemblages. Furthermore, authigenic clay minerals can also interfere with paleo-climatic and paleo-environmental signals based on detrital clay minerals (Chamley, 1989; Song et al., 2018; Wang et al., 2020). The scanning electron microscope (SEM) observation results (Fig. 5H, I) indicate that most clay particles usually show irregular shapes and rounded outlines, implying a detrital origin rather than an authigenic origin.

5.2. Provenance of the analyzed lacustrine siliciclastic sediments

The potential parent-rock lithological differences in detritus sources and the sediment generation, erosion and transport processes may significantly influence weathering products and thus sediment compositions (Singer, 1984; Fagel, 2007). Therefore, sediment provenance should be interpreted before discussing the paleo-climatic and paleo-environmental implications of detrital clay minerals and fine-grained siliciclastic sediment geochemical compositions. Some trace elements (e.g., Th and Sc) and REEs have been regarded as useful tracers for interpreting parent-rock composition of sediments (Taylor and McLennan, 1985; McLennan, 1989). In addition, Nd isotopic compositions of fine-grained sediments have been successfully used in provenance studies (e.g., Kuhlmann et al., 2004; Jian et al., 2020b; Chaudhuri et al., 2021). Our results show that the analyzed sediments have first-cycle (or unobvious recycling) sedimentation characteristics based on the Zr/Sc vs. Th/Sc plot (Fig. 9A). Our data indicate that the Th/Sc and La/Th ratios and the εNd(0) values of the analyzed samples maintain fairly small ranges and are almost unchanged in the ~13.4 Ma–12 Ma and ~9.2 Ma–8.4 Ma intervals (Fig. 7). This means that the geochemical compositions of their parent-rocks probably remained invariable in these two periods. All the sample data are plotted into similar fields in the La-Th-Sc ternary diagram (Fig. S4 in Appendix B) and are close to the La apex and far away from the Sc apex, reflecting a predominant felsic source composition (McLennan, 1989, 1993). The dominant felsic parent-rocks are also supported by low La/Th ratios (varying from 2.08 to 2.78, averaging 2.38) and the REE patterns of these samples which resemble PAAS compositions (Gd_N/Yb_N = 1.0–2.0 and Eu/Eu* < 0.85; Fig. 9B–D).

Most studies suggest that the Eastern Kunlun, Qilian and Altyn Tagh Mountains were the main potential detrital sources for the Cenozoic Qaidam basin (e.g., Cheng et al., 2016; Wang et al., 2017; Zhu et al., 2017; Lu et al., 2018; Song et al., 2019; Hong et al., 2020). We note that the Qilian and Eastern Kunlun Mountains have experienced different tectono-magmatic evolution (Jian et al., 2020a; Zhang et al., 2021) and thus the bedrock therein displays different formation age populations and Nd isotopic compositions (Wu et al., 2010). Previous studies have shown that the Altyn Tagh Mountains are featured by a left-lateral strike-slip fault (i.e., the Altyn Tagh Fault) and have similar rock assemblages to both the Qilian and Eastern Kunlun Mountains (Gehrels et al., 2003). Therefore, we employed Nd isotope tracers to model contributions from the potential sediment sources. We chose the data of modern fluvial sediments from the Qilian Mountains (εNd (0) = −12.49, $QL_{\varepsilon Nd(0)}$, average value of 8 samples, see Fig. S5 in Appendix B for sample locations; Wu et al. (2010)) and Eastern Kunlun-Qaidam (εNd(0) = −8.30, $EKQ_{\varepsilon Nd(0)}$, average value of 5 samples, see Fig. S5 in Appendix B for sample locations; Wu et al. (2010)) as two end members for a simple mixing model calculation. The modeling results are exhibited in Table 1. Results show that the analyzed sediments are mixed by 31 %–47 % Qilian-end-member and 53 %–69 % Eastern Kunlun-Qaidam-end-member materials (Table 1). Variations in contributions by these two end-members are in a small range (16 %), revealing that the Xiaoliangshan sediments were potentially derived from relatively stable sources or fed by well-mixed detritus from contribution-fixed sources. The results of Nd isotopic analysis and corresponding interpretations are consistent with the trace- and rare earth element records (Fig. 7). Note that the modeling results do not mean that the siliciclastic sediments were only from the Qilian and Eastern Kunlun Mountains. These sediments could also be derived from Qilian- or Eastern Kunlun-compositionally equivalent rocks.

5.3. Paleo-weathering intensity recorded by clay minerals and siliciclastic geochemical compositions of the lacustrine deposits

The composition and crystallization characteristics of clay minerals are reliable proxies for paleo-weathering reconstruction. It is well known that increasing Ka/I ratios and illite chemistry index (illite 5 Å/10 Å) values commonly indicate intensification of chemical weathering. The illite chemistry index drops when elements Mg and Fe take the place of Al in the crystal lattice. Al-rich illite, which is a product of intense hydrolysis, displays high values of the illite chemistry index, whereas the Fe-Mg-rich illite, which is regarded as a signal of intense physical erosion, has low illite chemistry index values (Y. Gao et al., 2021). The illite chemistry index data indicate that the types of illite in all the samples are mainly Fe-Mg-rich illite (Fig. 7). Overall, the low values of Ka/I (0.02–0.19) and illite 5 Å/10 Å (0.13–0.45) proxies demonstrate overwhelmingly mild chemical weathering intensity. The N_2^2 samples have stable Ka/I value, whereas these ratios are more variable and display a slightly increasing trend during ~8.8–8.4 Ma after a slight decline during ~9.2–8.8 Ma for N_2^3 samples (Fig. 8A). However, the illite 5 Å/10 Å values are highly fluctuant in these analyzed N_2^2 and N_2^3 samples (Fig. 8B). The illite 5 Å/10 Å values of the N_2^3 samples also display a decreasing tendency followed by an increase, similar to the Ka/I ratios (Fig. 8B). These variations in Ka/I and illite 5 Å/10 Å values indicate that the N_2^3 sediments experienced a gradual weakening of chemical weathering intensity during ~9.2–8.8 Ma, followed by relatively strong chemical weathering intensity during ~8.8–8.4 Ma.

Major elemental data plotted in the A-CN-K diagram exhibit an ideal weathering trend (Fig. S6 in Appendix B), which indicates little occurrence of diagenetic K-metasomatism (Fedo et al., 1995) and relatively stable (or well-mixed) sediment parent-rock types. This is also consistent with the above interpretations about the clay mineral formation and provenance. Overall, the corrected CIA (60.6–66.3, avg. = 63.6) values of the analyzed samples indicate mild-moderate chemical weathering conditions (Fig. 8D), consistent with the results of clay mineralogical proxies (Figs. 8A, B, 10B, C). Similar mild-moderate chemical weathering conditions (CIA values) were observed in late Miocene sediments from the northern Qaidam basin (Jian et al., 2013; Ren et al., 2019, 2020; Fu et al., 2022). For the ~13.4–12 Ma and ~8.8–8.4 Ma samples, the increasing corrected CIA values show strengthening chemical weathering (Fig. 8D).

5.4. Environmental significance of clay minerals and geochemical weathering indices compared with other proxies

5.4.1. Controls on clay minerals and geochemical compositions of the lacustrine siliciclastic deposits

We compared our chemical weathering records with paleo-climate records from other indicators (Fig. 8). Sedimentary carbonate $\delta^{18}O$ ($\delta^{18}_{carb}O$) data from Wells L101 and L6 were previously used to evaluate paleo-lake hydrology (Jian et al., 2014). High $\delta^{18}_{carb}O$ values represent intensive evaporation environments (Jian et al., 2014). The

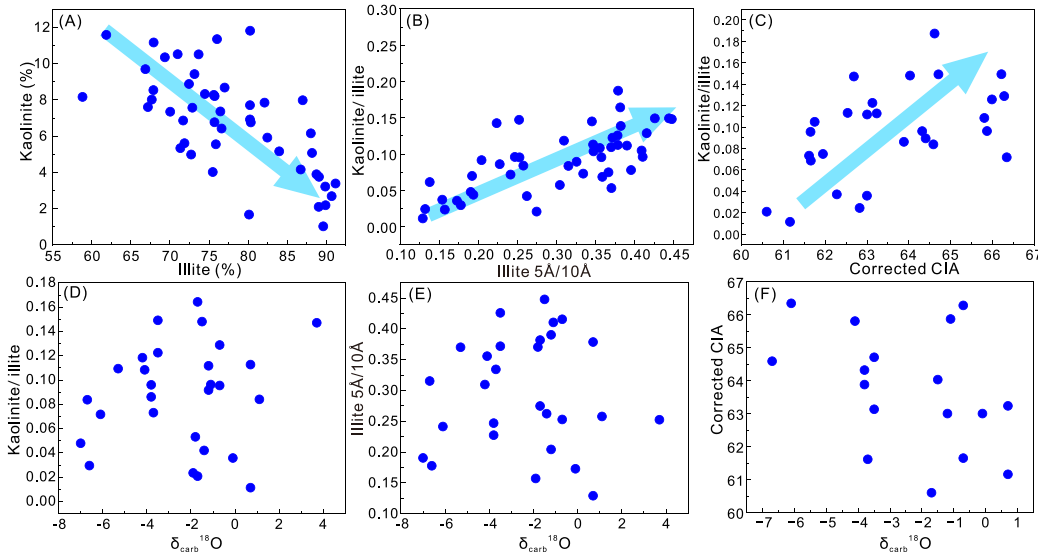

Fig. 10. Relationships between clay mineralogical indices, corrected CIA and sedimentary carbonate $\delta^{18}O$ ($\delta^{18}_{carb}O$). Note that all the siliciclastic sediment proxies (kaolinite/illite, illite 5 Å/10 Å and corrected CIA values) have no correlation with the sedimentary carbonate $\delta^{18}O$ ($\delta^{18}_{carb}O$) values.

positive ~2.5 ‰ shift in the most negative $\delta^{18}_{carb}O$ values after ~9.2 Ma was explained by strengthened aridity (Fig. 8E) (Jian et al., 2014). This is reinforced by the increasing evaporite mineral contents (Fig. 8F) (W. Zhang et al., 2018). High terrigenous/aquatic ratio (TAR = (C_{27} + C_{29} + C_{31}) / (C_{15} + C_{17} + C_{19}) of the n-alkanes) values indicate relatively low lake level (Fig. 8G) (Liang et al., 2021), coincided with dry climatic conditions as inferred from increasing xerophytic percentages and decreasing percentages of humid conifers (Fig. 8H, I) (Miao et al., 2013). The increasing aridification in Central Asia (including the western Qaidam basin) since the late Miocene is also well supported by evidence from aeolian sediments (An et al., 2001; Song et al., 2007), isotopic data (Zhuang et al., 2011a), sedimentological and geochemical records (Song et al., 2014; Yang et al., 2019). The overall mild-moderate chemical weathering condition and weakening of chemical weathering intensity during ~9.2–8.8 Ma reconstructed in this study and other weathering intensity reconstruction results of the Qaidam basin (e.g., Jian et al., 2013; Ren et al., 2019; Yin et al., 2019; Fu et al., 2022) seem to be consistent with the long-term regional aridification in Central Asia (also including the northern Tibetan Plateau) and with the global cooling during the late Cenozoic (Guo et al., 2002; Chang et al., 2008; Miao et al., 2013; Bao et al., 2019). However, our new data show two periods of abnormally enhanced chemical weathering during ~13.4–12 Ma and ~8.8–8.4 Ma (Fig. 8A–D), which is surprisingly decoupled with the intensified regional aridity in the western Qaidam basin. This can be explained as follows.

It is widely accepted that clay minerals and geochemical compositions of lacustrine siliciclastic sediments may be controlled by the factors and processes within sediment source-to-sink systems (e.g., parent-rock lithology, topography, climate, weathering and hydrodynamics) (Nesbitt and Young, 1982; Bhatia and Crook, 1986; Fedo et al., 1995; Garzanti et al., 2011; Jian et al., 2013; Liu et al., 2016). As discussed above, parent-rocks of the analyzed sediments are mainly felsic rocks and chemical compositions of the parent-rocks remain nearly invariable during the late Miocene. We note that there existed a unified megalake in the Qaidam basin during the middle–late Miocene and the depocenter of this megalake was mainly located in the western part of the basin during much of the Cenozoic time (Wang et al., 2006; Yin et al., 2008; Zhuang et al., 2011b; Mao et al., 2014; Guo et al., 2018). Furthermore, rather than siliciclastic rock-dominated records, carbonate- and evaporite-rich mixed sedimentary rocks are widely distributed in the Miocene strata in this region, implying underdeveloped fluvial-delta systems and relatively low clastic sediment flux in the western Qaidam basin (Fig. 11) (Jian et al., 2014; Song et al., 2014; Chang et al., 2015). By contrast, the late Cenozoic northern and eastern Qaidam basin are broadly dominated by fluvial-delta and marginal lake siliciclastic deposits (Fig. 2) and indicate high clastic sediment flux from adjacent sources (Fig. 11) (Zhuang et al., 2011b; Ji et al., 2017; Fu et al., 2022). Paleo-current orientation measurement results indicate general west-southwest- and north-, northeast-directed paleo-flow for most areas in the Qaidam basin (except some measuring sections close to the Altyn Tagh Mountains) during the megalake period (Zhuang et al., 2011b; Xia et al., 2021). All the evidence implies that the western Qaidam basin sediments, especially for those fine-grained siliciclastic deposits in relatively deep lake environments, were not only fed by the proximal Altyn Tagh Mountains, but could also be derived from source areas to the north, south and east during the late Cenozoic. In addition, because the eastern Qaidam basin was prone to the influence of the East Asian monsoon whereas the western Qaidam basin was under the control of the Westerlies (M. Wu et al., 2019), the climate in the eastern Qaidam basin is thought to be wetter than that in the western Qaidam basin and the chemical weathering intensity documented in eastern Qaidam basin is found to be relatively stronger than that in the western Qaidam basin (Jian et al., 2013; Ren et al., 2019; M. Wu et al., 2019). We also note that the Cenozoic tectonic activity (e.g., crustal thickening, uplift and exhumation) in the Qilian Mountains (and also in other areas of the northeastern Tibet) reached its peak at 13–12 Ma (Li et al., 2020). Therefore, enhanced erosion in the eastern sources is expected to result in higher more-weathered material supply into the Qaidam basin than that in the western source regions. This east-derived fine-grained detritus could be transported through lake current and deposited in the western Qaidam basin. As a result, the analyzed fine-grained sediments show comparatively stronger chemical weathering alteration during ~13.4 Ma to 12 Ma (Fig. 8D). Although several studies on Cenozoic sandstones advocate dominant contributions of the Altyn Tagh Mountains and the west part (i.e., the Qimantagh area) of the Eastern Kunlun Mountains to the western Qaidam basin (Rieser et al., 2005; Cheng et al., 2016; Zhu et al., 2017), we realize that different sources and transport pathways for sandy and muddy sediments in a sedimentary depocenter are quite common (Nelson and Lister, 2010; Shen et al., 2021).

Coincidentally, a growing number of studies suggest intensified East Asian summer monsoon (EASM) precipitation in the northeastern Tibet

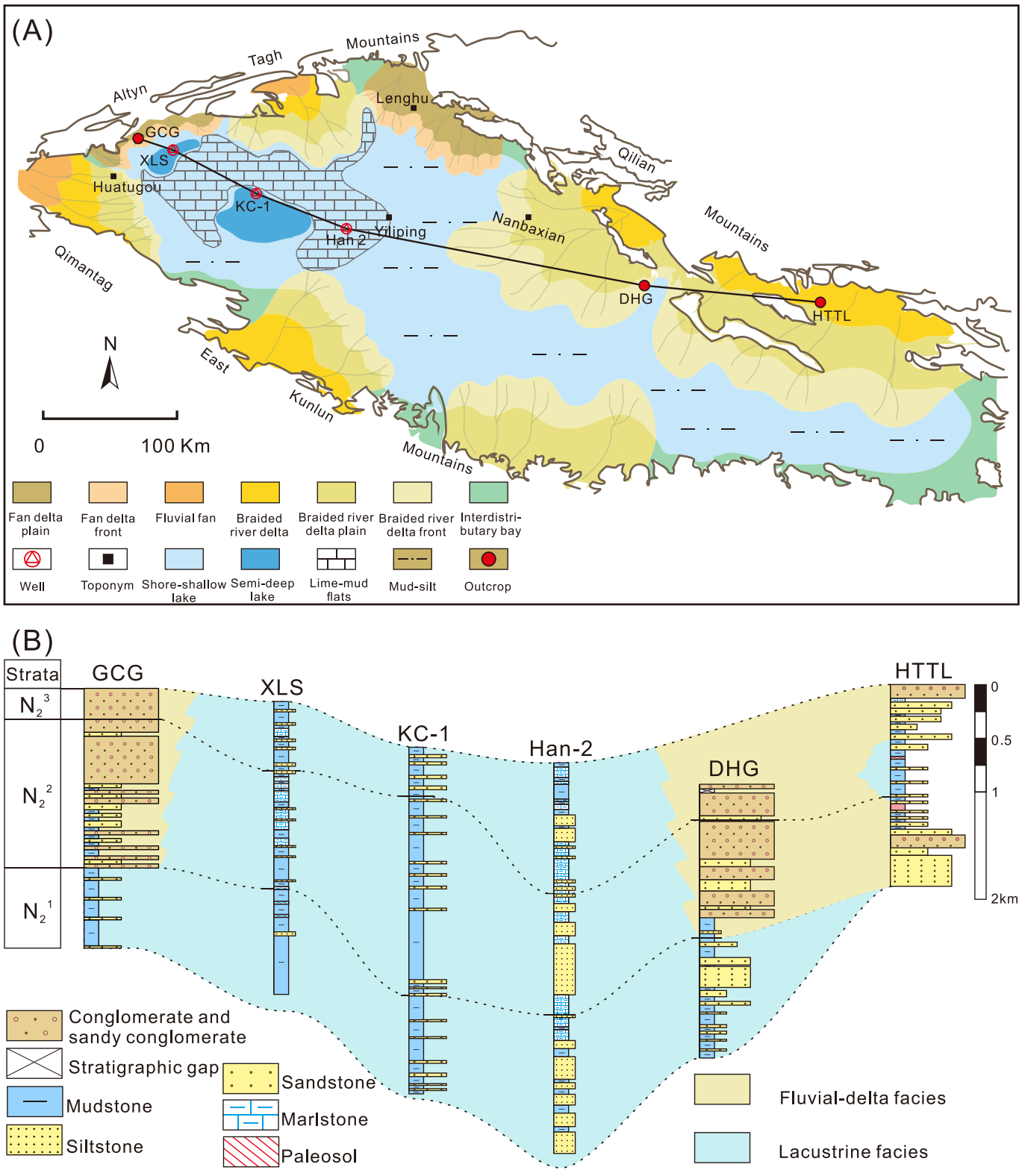

Fig. 11. (A) Paleo-geographic environment of the Qaidam basin during the Miocene, modified from Song et al. (2022). (B) Representative outcrop and borehole stratigraphic profiles in the Qaidam basin, showing lithological records and sedimentary facies evolution of the Miocene megalake. It's worth noting that the sedimentary carbonate-rich rocks, instead of siliciclastic rock-dominated records, are widely distributed in the western Qaidam basin during the Miocene, implying underdeveloped fluvial-delta systems and relatively low clastic sediment flux in the western Qaidam basin. In contrast, the northern and eastern Qaidam basin were broadly dominated by fluvial-delta and marginal lake deposits and accumulated abundant clastic sediments from adjacent sources. Lithological columns are modified from Guan and Jian (2013) for GCG and LLH, from Wang et al. (2012) for XLS, from unpublished reports by the Qinghai Oil Company for Han-2, from Liang et al. (2021) for KC-1 and DHG, and from Fu et al. (2022) for HTTL. N_2^3: Shizigou Formation; N_2^2: Shangyoushashan Formation; N_2^1: Xiayoushashan Formation; GCG: Ganchaigou; XLS: Xiaoliangshan; DHG: Dahonggou; HTTL: Huaitoutala.

regions during the late Miocene (e.g., during 8.5–7 Ma in the northeastern Qaidam basin (Nie et al., 2017, 2019), before ~8.57 Ma in the Jianzha basin (Fu et al., 2018) and during ~7.4–6.1 Ma in the Tianshui basin (Hui et al., 2021)). The CIA values of fine-grained sedimentary rocks from the northeastern Qaidam basin also reveal the corresponding relation between increased chemical weathering strength and intensified EASM precipitation during 9 Ma to 6 Ma (Fu et al., 2022). The clay minerals in the modern river sediments from the Qilian Mountains and in the late Cenozoic sediments from the northeastern Qaidam basin are dominated by illite and chlorite (Miao et al., 2016; Liang, 2019), consistent with the clay mineralogical results in this study. Differences in geological background and climatic conditions of those river catchments might contribute to the fluctuant clay mineral assemblages and illite chemistry index (Opitz et al., 2016; Liang, 2019). Significant detritus contributions from the eastern sediment sources in the northeastern Tibet to the western Qaidam basin during the late Cenozoic, if reasonable, could lead to variations in paleo-weathering records in the far west depocenters. In this case, the two periods of abnormally enhanced chemical weathering documented in the Xiaoliangshan siliciclastic strata might reflect the influences of tectonic and climatic changes in the eastern Qaidam basin and even in the mountains around the northeast margin of the Tibetan Plateau during ~13.4–12 Ma and ~8.8–8.4 Ma. We realize that shorter timescale weathering records in this region are also crucial to better understand the interactions among tectonics, climate and basin sedimentation process (B. Song et al., 2013; Ren et al., 2020). However, limited to the low sampling resolution and the discontinuous rock core collection processes, short timescale chemical weathering variation history cannot be determined in this study. The strong fluctuations in clay mineral assemblages among adjacent samples might also be related to short timescale climate variations (such as the Milankovitch climate cycles) in the northeastern Tibetan Plateau, which have been well recognized in several recent studies (Nie et al., 2017; Wang et al., 2019; P. Gao et al., 2021; Yao et al., 2022).

On the whole, this speculation seems plausible and is consistent with most provenance, sedimentological and climatic evidence. We suggest that clay mineralogical and geochemical compositions of lacustrine fine-grained siliciclastic deposits were strongly controlled by the whole sediment source-to-sink processes, rather than the local climatic or environmental conditions of the depositional regions. Given the occurrence of the Miocene megalake in the Qaidam basin (Guo et al., 2018; Liang et al., 2021), sediment transport pathways and water dynamics (e.g., the lake currents) within the lacustrine environments might play a crucial role in redistribution of the fine-grained sediments and further in controlling the clay mineralogical and geochemical compositions. Some present-day megalake cases also highlight the significant roles of lake currents in sediment transport processes (Ulmann et al., 2003; Nutz et al., 2015; T. Wu et al., 2019).

5.4.2. Differences in sediment-related paleo-climate and paleo-environment indicators

Some case studies demonstrate that paleo-climate records obtained from clay mineralogical and geochemical compositions of fine-grained siliciclastic sediments are consistent with those obtained by other methods in terrestrial and marine deposits (e.g., Zhang et al., 2015, 2016; Yang et al., 2019; Wang et al., 2020). In this study, however, the paleo-weathering interpretations based on clay mineral and geochemical compositions of the analyzed ~13.4–12 Ma and 8.8–8.4 Ma lacustrine siliciclastic deposits are uncorrelated with previous climate interpretations (Figs. 8, 10D–F). These paleo-climate studies were based on sedimentary carbonate $\delta^{18}O$ ($\delta^{18}_{carb}O$), evaporite-related lithofacies and biomarker (terrigenous/aquatic ratio, named as TAR = $(C_{27} + C_{29} + C_{31}) / (C_{15} + C_{17} + C_{19})$ of the n-alkanes) data which display a trend of intensified regional aridity in the western Qaidam basin during the middle–late Miocene (Fig. 8E–G) (Jian et al., 2014; W. Zhang et al., 2018; Liang et al., 2021). Indeed, sedimentary carbonate oxygen isotopes and evaporite mineral contents are usually applied to reflect lake hydrological conditions (Jian et al., 2014; Guo et al., 2018; Mccormack et al., 2019). Autochthonous biomarkers serve as paleo-climate and paleo-environment proxies according to their suitability for different paleo-climate parameters and aquatic environments (e.g., water temperature) (Regnery et al., 2013). Therefore, the sedimentary carbonate oxygen isotopes, evaporite minerals and autochthonous biomarkers are native to the lake, and thus can represent the local climatic conditions within the confines of the lake (Jian et al., 2014; Ouyang et al., 2015; L. Li et al., 2017; Pu et al., 2017).

Our records in these periods are also discrepant with sporopollen records from the borehole KC-1 near the study area (see Fig. 1B for location) which reveal continuous aridification in the western Qaidam basin (Fig. 8H, I) (Miao et al., 2013). Although most sporopollens are thought to be deposited near plants (Hui et al., 2011; Wu et al., 2014), a considerable portion of sporopollens may also be transported to much broader regions (e.g., 120 km–180 km or further) by winds and rivers (Wu et al., 2013). Thus, sporopollen records are more suitable for regional paleo-environment reconstruction, with larger spatial scales than watershed or lake ranges (Meyers, 2003; Regnery et al., 2013). By contrast, as discussed above, siliciclastic sediments in lakes (especially in megalakes) are controlled by parent-rock compositions from source regions and can also be impacted by the whole sediment source-to-sink processes (e.g., weathering, transport and deposition). These kinds of records tend to reflect environmental change involving watershed and lake systems.

In summary, there are at least three types of paleo-climatic proxies from the middle–late Miocene Qaidam paleo-megalake sediments which may produce distinct paleo-climatic interpretations (Fig. 12). These include (1) authigenic sedimentary mineral and aquatic organism-related biomarker proxies, reflecting hydrological and climatic conditions in localized areas where lacustrine sediments accumulated (e.g., lake); (2) siliciclastic sediment proxies, highlighted in this study, indicating climatic conditions in lake and potential drainage areas (involving northeastern Tibetan Plateau) where the detrital materials were produced, weathered, transported and deposited; (3) allochthonous, water-unrelated component (e.g., wind-carried particles) proxies, reflecting climatic conditions in much broader regions, such as the whole Central Asia.

5.5. Implications

Lacustrine and marine sedimentary successions are important archives for paleo-climate research (Zachos et al., 2008; Grotzinger et al., 2015; Ouyang et al., 2015). Numerous sediment-related proxies, such as grain size, isotopic tracers (e.g., sedimentary carbonate $\delta^{18}O$ and $\delta^{13}C$ values), elemental compositions (e.g., major-, trace- and rare earth elements), carbonate contents, clay minerals, sporopollens, biomarker compositions (e.g., n-alkanes) and magnetic susceptibility have been widely applied in paleo-climate and paleo-environment reconstructions (e.g., Chen et al., 2004; Zhang and Mischke, 2009; Grotzinger et al., 2015; Ouyang et al., 2015; Nie et al., 2017; Liang et al., 2021). The results in this study indicate distinct paleo-climate significances between siliciclastic sediment-related proxies and other sediment components-related proxies for the Qaidam paleo-lake. This means that depositional processes of different components in sedimentary records should be concerned before paleo-climate interpretations, especially for those complex megalake or marine sedimentary systems. Our findings underline the importance of a sediment source-to-sink perspective for paleo-climate study based on siliciclastic archives in megalake.

6. Conclusions

In this study, we targeted the late Cenozoic lacustrine strata from the northwestern Qaidam basin, to better understand paleo-megalake

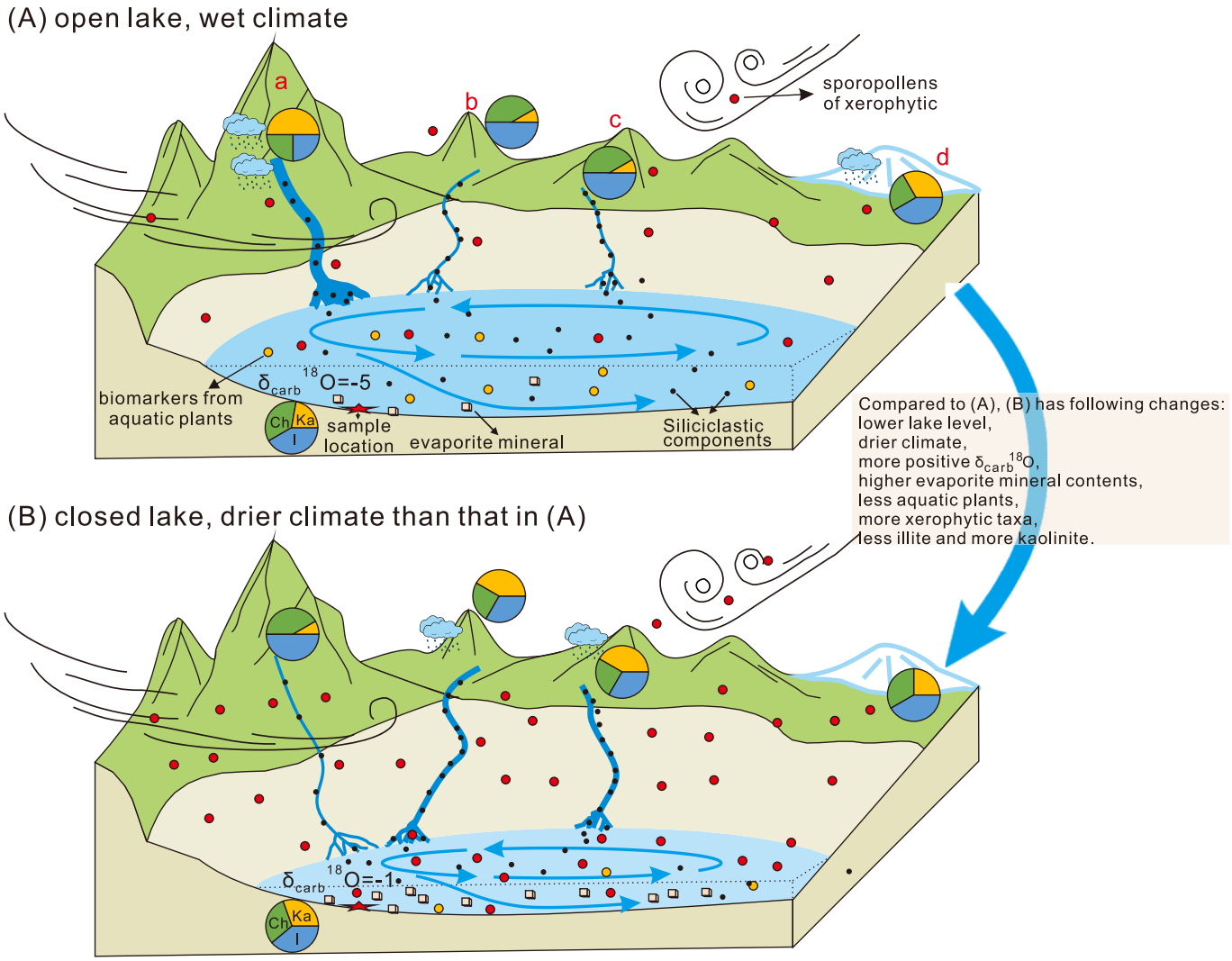

Fig. 12. Schematic diagrams showing controls on the diverse paleo-climatic proxies based on different sediment components (including siliciclastic components, e.g., clay minerals; biological components, e.g., sporopollens of land plants and biomarkers from aquatic plants; and authigenic mineral components, e.g., sedimentary carbonate and evaporite minerals) in a megalake sedimentary system. These illustrations can explain why clay mineralogical and geochemical records are different from other sediment component records and explain how the reconstructed paleo-weathering intensity is decoupled with local climate change in the northwestern Qaidam basin. The two distinct climatic conditions resulted in different behaviors of the climate proxies. The lake deposits indicate relatively high carbonate $\delta^{18}O$ ($\delta^{18}_{carb}O$) values and evaporite mineral contents due to the local lake aridity. Sporopollen (e.g., increasing xerophytic) from source areas a, b, c and d record the increasing regional aridity. However, proxies based on siliciclastic fractions (e.g., clay minerals) vary differently, documenting climate changes involving source drainage areas (a, b and c), transport pathways and depositional regions. This schematic diagram highlights the significance of a sediment source-to-sink system perspective when targeting siliciclastic materials from megalake systems in paleo-climate studies.

sedimentary records of weathering and climate in a relatively arid, tectonically active region. Results indicate that the chemical weathering intensity history documented in the megalake fine-grained siliciclastic sediments was decoupled with local climate evolution in the northwestern Qaidam basin. The highly fluctuant clay mineralogical and element geochemical records and the corresponding variation trends are different from other sedimentary component-based (e.g., authigenic minerals and organic materials) proxy data, implying dissimilar paleo-climate interpretations. We suggest that the variations in the paleo-megalake fine-grained siliciclastic sediment compositions were attributed to weathering, tectonic and climatic conditions in their source regions, transport pathways and depositional areas, rather than the local climate.

CRediT authorship contribution statement

Ling Wang: Conceptualization, Data curation, Investigation, Writing – original draft. **Xing Jian:** Conceptualization, Data curation, Investigation, Writing – review & editing. **Hanjing Fu:** Investigation, Data curation, Visualization. **Wei Zhang:** Investigation, Project administration. **Fei Shang:** Investigation, Resources. **Ling Fu:** Investigation, Resources.

Data availability

Data are available on request from the authors.

Declaration of competing interest

The authors declare that they have no known competing financial interests or personal relationships that could have appeared to influence the work reported in this paper.

Acknowledgments

This research was supported by the National Natural Science Foundation of China (No. 41902126) and Xiamen University Fundamental Research Funds for the Central Universities (No. 20720160114). We appreciate the Qinghai Oilfield Company for assistance and support during

the sampling. Acknowledgment goes to the Editor Catherine Chagué and two anonymous reviewers for critical and constructive feedback that was extremely helpful in improving an earlier version of this manuscript.

Supplementary data

Supplementary data to this article can be found online at https://doi.org/10.1016/j.sedgeo.2023.106462.

References

An, Z., Kutzbach, J.E., Prell, W.L., Porter, S.C., 2001. Evolution of Asian monsoons and phased uplift of the Himalaya–Tibetan plateau since Late Miocene times. Nature 411, 62–66.

Bao, J., Wang, Y., Song, C., Feng, Y., Hu, C., Zhong, S., Yang, J., 2017. Cenozoic sediment flux in the Qaidam Basin, northern Tibetan Plateau, and implications with regional tectonics and climate. Global and Planetary Change 155, 56–69.

Bao, J., Song, C., Yang, Y., Fang, X., Meng, Q., Feng, Y., He, P., 2019. Reduced chemical weathering intensity in the Qaidam Basin (NE Tibetan Plateau) during the Late Cenozoic. Journal of Asian Earth Sciences 170, 155–165.

Bhatia, M.R., Crook, K.A.W., 1986. Trace element characteristics of graywackes and tectonic setting discrimination of sedimentary basins. Contributions to Mineralogy and Petrology 92, 181–193.

Biscaye, P.E., 1965. Mineralogy and sedimentation of recent deep-sea clay in the Atlantic Ocean and adjacent seas and oceans. Geological Society of America Bulletin 76, 803–832.

Bock, B., Mclennan, S.M., Hanson, G.N., 1998. Geochemistry and provenance of the Middle Ordovician Austin Glen Member (Normanskill Formation) and the Taconian Orogeny in New England. Sedimentology 45, 635–655.

Bouchez, J., Gaillardet, J., France-Lanord, C., Maurice, L., Dutra-Maia, P., 2011. Grain size control of river suspended sediment geochemistry: clues from Amazon River depth profiles. Geochemistry, Geophysics, Geosystems 12, Q03008. https://doi.org/10.1029/2010gc003380.

Bush, M.A., Saylor, J.E., Horton, B.K., Nie, J., 2016. Growth of the Qaidam Basin during Cenozoic exhumation in the northern Tibetan Plateau: inferences from depositional patterns and multiproxy detrital provenance signatures. Lithosphere 8, 58–82.

Chamley, H., 1989. Clay Sedimentology. Springer-Verlag, Heidelberg (623 pp.).

Chang, M., Wang, X., Liu, H., Miao, D., Zhao, Q., Wu, G., Liu, J., Li, Q., Sun, Z., Wang, N., 2008. Extraordinarily thick-boned fish linked to the aridification of the Qaidam Basin (northern Tibetan Plateau). Proceedings of the National Academy of Sciences 105, 13246. https://doi.org/10.1073/pnas.0805982105.

Chang, H., Li, L., Qiang, X., Garzione, C.N., Pullen, A., An, Z., 2015. Magnetostratigraphy of Cenozoic deposits in the western Qaidam Basin and its implication for the surface uplift of the northeastern margin of the Tibetan Plateau. Earth and Planetary Science Letters 430, 271–283.

Chaudhuri, A., Chatterjee, A., Banerjee, S., Ray, J.S., 2021. Tracing multiple sources of sediments using trace element and Nd isotope geochemistry: provenance of the Mesozoic succession in the Kutch Basin, western India. Geological Magazine 158, 359–374.

Chen, J., Wan, G., Zhang, D., Zhang, F., Huang, R., 2004. Environmental records of lacustrine sediments in different time scales: sediment grain size as an example. Science in China, Series D: Earth Sciences 47, 954–960.

Cheng, F., Fu, S., Jolivet, M., Zhang, C., Guo, Z., 2016. Source to sink relation between the Eastern Kunlun Range and the Qaidam Basin, northern Tibetan Plateau, during the Cenozoic. Geological Society of America Bulletin 128, 258–283.

Cheng, F., Jolivet, M., Guo, Z., Wang, L., Zhang, C., Li, X., 2021. Cenozoic evolution of the Qaidam basin and implications for the growth of the northern Tibetan plateau: a review. Earth-Science Reviews 220, 103730. https://doi.org/10.1016/j.earscirev.2021.103730.

Deconinck, J., Hesselbo, S.P., Pellenard, P., 2019. Climatic and sea-level control of Jurassic (Pliensbachian) clay mineral sedimentation in the Cardigan Bay Basin, Llanbedr (Mochras Farm) borehole, Wales. Sedimentology 66, 2769–2783.

Dellisanti, F., Pini, G.A., Baudin, F., 2010. Use of Tmax as a thermal maturity indicator in orogenic successions and comparison with clay mineral evolution. Clay Minerals 45, 115–130.

Dinis, P., Garzanti, E., Vermeesch, P., Huvi, J., 2017. Climatic zonation and weathering control on sediment composition (Angola). Chemical Geology 467, 110–121.

Dinis, P., Garzanti, E., Hahn, A., Vermeesch, P., Cabral-Pinto, M., 2020. Weathering indices as climate proxies. A step forward based on Congo and SW African river muds. Earth-Science Reviews 201, 103039. https://doi.org/10.1016/j.earscirev.2019.103039.

Ehrmann, W., Setti, M., Marinoni, L., 2005. Clay minerals in Cenozoic sediments off Cape Roberts (McMurdo Sound, Antarctica) reveal palaeoclimatic history. Palaeogeography, Palaeoclimatology, Palaeoecology 229, 187–211.

Fagel, N., 2007. Chapter four clay minerals, deep circulation and climate. In: Hillaire-Marcel, C., De Vernal, A. (Eds.), Developments in Marine Geology. Elsevier, Amsterdam, pp. 139–184.

Fang, X., Zhang, W., Meng, Q., Gao, J., Wang, X., King, J., Song, C., Dai, S., Miao, Y., 2007. High-resolution magnetostratigraphy of the Neogene Huaitoutala section in the eastern Qaidam Basin on the NE Tibetan Plateau, Qinghai Province, China and its implication on tectonic uplift of the NE Tibetan Plateau. Earth and Planetary Science Letters 258, 293–306.

Fedo, C.M., Wayne Nesbitt, H., Young, G.M., 1995. Unraveling the effects of potassium metasomatism in sedimentary rocks and paleosols, with implications for paleoweathering conditions and provenance. Geology 23, 921–924.

Floyd, P.A., Leveridge, B.E., 1987. Tectonic environment of the Devonian Gramscatho basin, South Cornwall: framework mode and geochemical evidence from turbiditic sandstones. Journal of Geological Society 144, 531–542.

Fu, C., Qiang, X., Xu, X., Xi, J., Zuo, J., An, Z., 2018. Late Miocene magnetostratigraphy of Jianzha Basin in the northeastern margin of the Tibetan Plateau and changes in the East Asian summer monsoon. Geological Journal 53, 282–292.

Fu, H., Jian, X., Zhang, W., Shang, F., 2020. A comparative study of methods for determining carbonate content in marine and terrestrial sediments. Marine and Petroleum Geology 116, 104337. https://doi.org/10.1016/j.marpetgeo.2020.104337.

Fu, H., Jian, X., Liang, H., Zhang, W., Shen, X., Wang, L., 2022. Tectonic and climatic forcing of chemical weathering intensity in the northeastern Tibetan Plateau since the middle Miocene. CATENA 208, 105785. https://doi.org/10.1016/j.catena.2021.105785.

Gao, Y., Ibarra, D.E., Caves Rugenstein, J.K., Chen, J., Kukla, T., Methner, K., Gao, Y., Huang, H., Lin, Z., Zhang, L., Xi, D., Wu, H., Carroll, A.R., Graham, S.A., Chamberlain, C.P., Wang, C., 2021a. Terrestrial climate in mid-latitude East Asia from the latest Cretaceous to the earliest Paleogene: a multiproxy record from the Songliao Basin in northeastern China. Earth-Science Reviews 216, 103572. https://doi.org/10.1016/j.earscirev.2021.103572.

Gao, P., Nie, J., Yan, Q., Zhang, X., Liu, Q., Cao, B., Pan, B., 2021b. Millennial resolution Late Miocene northern China precipitation record spanning astronomical analogue interval to the future. Geophysical Research Letters 48, e2021GL093942. https://doi.org/10.1029/2021gl093942.

Garzanti, E., Andó, S., France-Lanord, C., Censi, P., Vignola, P., Galy, V., Lupker, M., 2011. Mineralogical and chemical variability of fluvial sediments 2. Suspended-load silt (Ganga–Brahmaputra, Bangladesh). Earth and Planetary Science Letters 302, 107–120.

Gehrels, G.E., Yin, A., Wang, X., 2003. Detrital-zircon geochronology of the northeastern Tibetan Plateau. Geologcal Society of America Bulletin 115, 881–896.

Grotzinger, J.P., Gupta, S., Malin, M.C., Rubin, D.M., Schieber, J., Siebach, K., Sumner, D.Y., Stack, K.M., Vasavada, A.R., Arvidson, R.E., Calef, F., Edgar, L., Fischer, W.F., Grant, J.A., Griffes, J., Kah, L.C., Lamb, M.P., Lewis, K.W., Mangold, N., Minitti, M.E., Palucis, M., Rice, M., Williams, R.M.E., Yingst, R.A., Blake, D., Blaney, D., Conrad, P., Crisp, J., Dietrich, W.E., Dromart, G., Edgett, K.S., Ewing, R.C., Gellert, R., Hurowitz, J.A., Kocurek, G., Mahaffy, P., McBride, M.J., McLennan, S.M., Mischna, M., Ming, D., Milliken, R., Newsom, H., Oehler, D., Parker, T.J., Vaniman, D., Wiens, R.C., Wilson, S.A., 2015. Deposition, exhumation, and paleoclimate of an ancient lake deposit, Gale crater. Mars. Science 350, aac7575. https://doi.org/10.1126/science.aac7575.

Guan, P., Jian, X., 2013. The Cenozoic sedimentary record in Qaidam Basin and its implications for tectonic evolution of the northern Tibetan Plateau. Acta Sedimentologica Sinica 35, 824–833 (in Chinese with English abstract).

Guan, C., Chang, H., Yan, M., Li, L., Xia, M., Zan, J., Liu, S., 2019. Rock magnetic constraints for the Mid-Miocene Climatic Optimum from a high-resolution sedimentary sequence of the northwestern Qaidam Basin, NE Tibetan Plateau. Palaeogeography, Palaeoclimatology, Palaeoecology 532, 109263. https://doi.org/10.1016/j.palaeo.2019.109263.

Guo, Z., Ruddiman, W., Hao, Q., Wu, H., Qiao, Y., Zhu, R., Peng, S., Wei, J., Yuan, B., Liu, T., 2002. Onset of Asian desertification by 22 Myr ago inferred from loess deposits in China. Nature 416, 159–163.

Guo, P., Liu, C., Huang, L., Yu, M., Wang, P., Zhang, G., 2018. Palaeohydrological evolution of the late Cenozoic saline lake in the Qaidam Basin, NE Tibetan Plateau: tectonic vs. climatic control. Global and Planetary Change 165, 44–61.

Hong, D., Jian, X., Fu, L., Zhang, W., 2020. Garnet trace element geochemistry as a sediment provenance indicator: an example from the Qaidam basin, northern Tibet. Marine and Petroleum Geology 116, 104316. https://doi.org/10.1016/j.marpetgeo.2020.104316.

Hui, Z., Li, J., Xu, Q., Song, C., Zhang, J., Wu, F., Zhao, Z., 2011. Miocene vegetation and climatic changes reconstructed from a sporopollen record of the Tianshui Basin, NE Tibetan Plateau. Palaeogeography, Palaeoclimatology, Palaeoecology 308, 373–382.

Hui, Z., Zhou, X., Chevalier, M., Wei, X., Pan, Y., Chen, Y., 2021. Miocene East Asia summer monsoon precipitation variability and its possible driving forces. Palaeogeography, Palaeoclimatology, Palaeoecology 581, 110609. https://doi.org/10.1016/j.palaeo.2021.110609.

Jacobsen, S.B., Wasserburg, G.J., 1980. Sm-Nd isotopic evolution of chondrites. Earth and Planetary Science Letters 50, 139–155.

Ji, J., Zhang, K., Clift, P.D., Zhuang, G., Song, B., Ke, X., Xu, Y., 2017. High-resolution magnetostratigraphic study of the Paleogene-Neogene strata in the Northern Qaidam Basin: implications for the growth of the Northeastern Tibetan Plateau. Gondwana Research 46, 141–155.

Jian, X., Guan, P., Zhang, W., Feng, F., 2013. Geochemistry of Mesozoic and Cenozoic sediments in the northern Qaidam basin, northeastern Tibetan Plateau: implications for provenance and weathering. Chemical Geology 360–361, 74–88.

Jian, X., Guan, P., Fu, S.-T., Zhang, D.-W., Zhang, W., Zhang, Y.-S., 2014. Miocene sedimentary environment and climate change in the northwestern Qaidam basin, northeastern Tibetan Plateau: facies, biomarker and stable isotopic evidences. Palaeogeography, Palaeoclimatology, Palaeoecology 414, 320–331.

Jian, X., Guan, P., Zhang, W., Liang, H., Feng, F., Fu, L., 2018. Late Cretaceous to early Eocene deformation in the northern Tibetan Plateau: detrital apatite fission track evidence from northern Qaidam basin. Gondwana Research 60, 94–104.

Jian, X., Weislogel, A., Pullen, A., Shang, F., 2020a. Formation and evolution of the Eastern Kunlun Range, northern Tibet: evidence from detrital zircon U-Pb geochronology and Hf isotopes. Gondwana Research 83, 63–79.

Jian, X., Zhang, W., Yang, S., Kao, S.-J., 2020b. Climate-dependent sediment composition and transport of mountainous rivers in tectonically stable, subtropical East

Asia. Geophysical Research Letters 47, e2019GL086150. https://doi.org/10.1029/2019GL086150.
Jian, X., Fu, L., Wang, P., Guan, P., Zhang, W., Fu, H., Mei, H., 2023. Sediment provenance of the Lulehe Formation in the Qaidam basin: insight to initial Cenozoic deposition and deformation in northern Tibetan plateau. Basin Research 35, 271–294.
Kuhlmann, G., de Boer, P.L., Pedersen, R.B., Wong, T.E., 2004. Provenance of Pliocene sediments and paleoenvironmental changes in the southern North Sea region using Samarium–Neodymium (Sm/Nd) provenance ages and clay mineralogy. Sedimentary Geology 171, 205–226.
Li, J., Tang, S., Zhu, X., Pan, C., 2017a. Production and certification of the reference material GSB 04-3258-2015 as a $^{143}Nd/^{144}Nd$ isotope ratio reference. Geostandards and Geoanalytical Research 41, 255–262.
Li, L., Wu, C., Fan, C., Li, J., Zhang, C., 2017b. Carbon and oxygen isotopic constraints on paleoclimate and paleoelevation of the southwestern Qaidam basin, northern Tibetan Plateau. Geoscience Frontiers 8, 1175–1186.
Li, M., Sun, S., Fang, X., Wang, C., Wang, Z., Wang, H., 2018. Clay minerals and isotopes of Pleistocene lacustrine sediments from the western Qaidam Basin, NE Tibetan Plateau. Applied Clay Science 162, 382–390.
Li, B., Zuza, A.V., Chen, X., Hu, D., Shao, Z., Qi, B., Wang, Z., Levy, D.A., Xiong, X., 2020. Cenozoic multi-phase deformation in the Qilian Shan and out-of-sequence development of the northern Tibetan Plateau. Tectonophysics 782–783, 228423. https://doi.org/10.1016/j.tecto.2020.228423.
Li, F., Yang, S., Breecker, D.O., Ramos, E.J., Huang, X., Duan, Z., Guo, Y., Li, C., Mei, X., 2022. Responses of silicate weathering intensity to the Pliocene-Quaternary cooling in East and Southeast Asia. Earth and Planetary Science Letters 578, 117301. https://doi.org/10.1016/j.epsl.2021.117301.
Liang, H., 2019. The Earth's Surface Chemical Weathering Intensity and Its Controlling Factors of Northern Qinghai-Tibet Plateau: Based on Cenozoic and Modern Sedimentary Records. (M.Sc. thesis)Xiamen University, Xiamen (in Chinese with English abstract).
Liang, Y., Zhang, B., Zhang, Y., Zhang, Y., Wang, J., Liu, Z., 2021. Evolution of the Miocene megalake in the western Qaidam Basin, northwestern China. Palaeogeography, Palaeoclimatology, Palaeoecology 571, 110384. https://doi.org/10.1016/j.palaeo.2021.110384.
Liu, Z., Colin, C., Huang, W., Le, K.P., Tong, S., Chen, Z., Trentesaux, A., 2007. Climatic and tectonic controls on weathering in South China and Indochina Peninsula: clay mineralogical and geochemical investigations from the Pearl, Red, and Mekong drainage basins. Geochemistry, Geophysics, Geosystems 8, Q05005. https://doi.org/10.1029/2006GC001490.
Liu, Z., Zhao, Y., Colin, C., Stattegger, K., Wiesner, M.G., Huh, C.-A., Zhang, Y., Li, X., Sompongchaiyakul, P., You, C.-F., Huang, C.-Y., Liu, J.T., Siringan, F.P., Le, K.P., Sathiamurthy, E., Hantoro, W.S., Liu, J., Tuo, S., Zhao, S., Zhou, S., He, Z., Wang, Y., Bunsomboonsakul, S., Li, Y., 2016. Source-to-sink transport processes of fluvial sediments in the South China Sea. Earth-Science Reviews 153, 238–273.
Lu, H., Xiong, S., 2009. Magnetostratigraphy of Dahonggou section, northern Qaidam Basin and its bearing on Cenozoic tectonic evolution of the Qilian Shan and Altyn Tagh Fault. Earth and Planetary Science Letters 288, 539–550.
Lu, H., Ye, J., Guo, L., Pan, J., Xiong, S., Li, H., 2018. Towards a clarification of the provenance of Cenozoic sediments in the northern Qaidam Basin. Lithosphere 11, 252–272.
Lupker, M., France-Lanord, C., Galy, V., Lavé, J., Kudrass, H., 2013. Increasing chemical weathering in the Himalayan system since the Last Glacial Maximum. Earth and Planetary Science Letters 365, 243–252.
Mao, L., Xiao, A., Wu, L., Li, B., Wang, L., Lou, Q., Dong, Y., Qin, S., 2014. Cenozoic tectonic and sedimentary evolution of southern Qaidam Basin, NE Tibetan Plateau and its implication for the rejuvenation of Eastern Kunlun Mountains. Science China Earth Sciences 57, 2726–2739.
Mccormack, J., Nehrke, G., Jöns, N., Immenhauser, A., Kwiecien, O., 2019. Refining the interpretation of lacustrine carbonate isotope records: implications of a mineralogy-specific Lake Van case study. Chemical Geology 513, 167–183.
McLennan, S.M., 1989. Chapter 7. Rare earth elements in sedimentary rocks: influence of provenance and sedimentary processes. In: Lipin, B.R., McKay, G.A. (Eds.), Geochemistry and Mineralogy of Rare Earth Elements. De Gruyter, Berlin, Boston, pp. 169–200.
McLennan, S.M., 1993. Weathering and global denudation. The Journal of Geology 101, 295–303.
McLennan, S.M., Hemming, S., McDaniel, D.K., Hanson, G.N., 1993. Geochemical approaches to sedimentation, provenance, and tectonics. Geological Society of America Special Paper 284, 21–40.
Mei, H., Jian, X., Zhang, W., Fu, H., Zhang, S., 2021. Behavioral differences between weathering and pedogenesis in a subtropical humid granitic terrain: implications for chemical weathering intensity evaluation. CATENA 203, 105368. https://doi.org/10.1016/j.catena.2021.105368.
Meng, Q.R., Fang, X., 2008. Cenozoic tectonic development of the Qaidam Basin in the northeastern Tibetan Plateau. Geological Society of America Special Paper 444, 1–24.
Meyers, P.A., 2003. Applications of organic geochemistry to paleolimnological reconstructions: a summary of examples from the Laurentian Great Lakes. Organic Geochemistry 34, 261–289.
Miao, Y., Fang, X., Herrmann, M., Wu, F., Zhang, Y., Liu, D., 2011. Miocene pollen record of KC-1 core in the Qaidam Basin, NE Tibetan Plateau and implications for evolution of the East Asian monsoon. Palaeogeography, Palaeoclimatology, Palaeoecology 299, 30–38.
Miao, Y., Fang, X., Wu, F., Cai, M., Song, C., Meng, Q., Xu, L., 2013. Late Cenozoic continuous aridification in the western Qaidam Basin: evidence from sporopollen records. Climate of the Past 9, 1863–1877.
Miao, W., Fan, Q., Wei, H., Zhang, X., Ma, H., 2016. Clay mineralogical and geochemical constraints on late Pleistocene weathering processes of the Qaidam Basin, northern Tibetan Plateau. Journal of Asian Earth Sciences 127, 267–280.
Nelson, C.S., Lister, G.S., 2010. Surficial bottom sediments of Lake Taupo, New Zealand: texture, composition, provenance, and sedimentation rates. New Zealand Journal of Geology and Geophysics 38, 61–79.
Nesbitt, H.W., Young, G.M., 1982. Early Proterozoic climates and plate motions inferred from major element chemistry of lutites. Nature 299, 715–717.
Nie, J., Garzione, C., Su, Q., Liu, Q., Zhang, R., Heslop, D., Necula, C., Zhang, S., Song, Y., Luo, Z., 2017. Dominant 100,000-year precipitation cyclicity in a late Miocene lake from Northeast Tibet. Science Advances 3, e1600762. https://doi.org/10.1126/sciadv.1600762.
Nie, J., Ren, X., Saylor, J.E., Su, Q., Horton, B.K., Bush, M.A., Chen, W., Pfaff, K., 2019. Magnetic polarity stratigraphy, provenance, and paleoclimate analysis of Cenozoic strata in the Qaidam Basin, NE Tibetan Plateau. Geological Society of America Bulletin 132, 310–320.
Nutz, A., Schuster, M., Ghienne, J.F., Roquin, C., Hay, M.B., Rétif, F., Certain, R., Robin, N., Raynal, O., Cousineau, P.A., SIROCCO Team, Bouchette, F., 2015. Wind-driven bottom currents and related sedimentary bodies in Lake Saint-Jean (Québec, Canada). Geological Society of America Bulletin 127, 1194–1208.
Opitz, S., Ramisch, A., Ijmker, J., Lehmkuhl, F., Mischke, S., Stauch, G., Wünnemann, B., Zhang, Y., Diekmann, B., 2016. Spatio-temporal pattern of detrital clay-mineral supply to a lake system on the north-eastern Tibetan Plateau, and its relationship to late Quaternary paleoenvironmental changes. CATENA 137, 203–218.
Ouyang, X., Guo, F., Bu, H., 2015. Lipid biomarkers and pertinent indices from aquatic environment record paleoclimate and paleoenvironment changes. Quaternary Science Reviews 123, 180–192.
Pu, Y., Wang, C., Meyers, P.A., 2017. Origins of biomarker aliphatic hydrocarbons in sediments of alpine Lake Ximencuo, China. Palaeogeography, Palaeoclimatology, Palaeoecology 475, 106–114.
Qiu, N., 2002. Tectono-thermal evolution of the Qaidam Basin, China: evidence from Ro and apatite fission track data. Petroleum Geoscience 8, 279–285.
Regnery, J., Püttmann, W., Koutsodendris, A., Mulch, A., Pross, J., 2013. Comparison of the paleoclimatic significance of higher land plant biomarker concentrations and pollen data: a case study of lake sediments from the Holsteinian interglacial. Organic Geochemistry 61, 73–84.
Ren, X., Nie, J., Saylor, J.E., Li, H., Bush, M.A., Horton, B.K., 2019. Provenance control on chemical weathering index of fluvio-lacustrine sediments: evidence from the Qaidam Basin, NE Tibetan Plateau. Geochemistry, Geophysics, Geosystems 20, 3216–3224.
Ren, X., Nie, J., Saylor, J.E., Wang, X., Liu, F., Horton, B.K., 2020. Temperature control on silicate weathering intensity and evolution of the Neogene East Asian summer monsoon. Geophysical Research Letters 47, e2020GL088808. https://doi.org/10.1029/2020GL088808.
Rieser, A.B., Neubauer, F., Liu, Y., Ge, X., 2005. Sandstone provenance of NORTH-western sectors of the intracontinental Cenozoic Qaidam basin, western China: tectonic vs. climatic control. Sedimentary Geology 177, 1–18.
Roddaz, M., Viers, J., Brusset, S., Baby, P., Boucayrand, C., Hérail, G., 2006. Controls on weathering and provenance in the Amazonian foreland basin: insights from major and trace element geochemistry of Neogene Amazonian sediments. Chemical Geology 226, 31–65.
Rudnick, R.L., Gao, S., 2003. Composition of the continental crust. In: Rudnick, R.L. (Ed.), The Crust. Elsevier, Amsterdam, pp. 1–64.
Shen, Z., Wang, M., Li, Y., Jackson, D.D., Yin, A., Dong, D., Fang, P., 2001. Crustal deformation along the Altyn Tagh fault system, western China, from GPS. Journal of Geophysical Research - Solid Earth 106, 30607–30621.
Shen, X., Jian, X., Li, C., Liu, J.T., Chang, Y.-P., Zhang, S., Mei, H., Fu, H., Zhang, W., 2021. Submarine topography-related spatial variability of the southern Taiwan Strait sands (East Asia). Marine Geology 436, 106495. https://doi.org/10.1016/j.margeo.2021.106495.
Singer, A., 1984. The paleoclimatic interpretation of clay minerals in sediments — a review. Earth-Science Reviews 21, 251–293.
Song, Y., Fang, X., Torii, M., Ishikawa, N., Li, J., An, Z., 2007. Late Neogene rock magnetic record of climatic variation from Chinese eolian sediments related to uplift of the Tibetan Plateau. Journal of Asian Earth Sciences 30, 324–332.
Song, S., Niu, Y., Su, L., Xia, X., 2013a. Tectonics of the North Qilian orogen, NW China. Gondwana Research 23, 1378–1401.
Song, B., Zhang, K., Lu, J., Wang, C., Xu, Y., 2013b. The middle Eocene to early Miocene integrated sedimentary record in the Qaidam Basin and its implications for paleoclimate and early Tibetan Plateau uplift. Canadian Journal of Earth Sciences 50, 183–196.
Song, C., Hu, S., Han, W., Zhang, T., Fang, X., Gao, J., Wu, F., 2014. Middle Miocene to earliest Pliocene sedimentological and geochemical records of climate change in the western Qaidam Basin on the NE Tibetan Plateau. Palaeogeography, Palaeoclimatology, Palaeoecology 395, 67–76.
Song, Y., Wang, Q., An, Z., Qiang, X., Dong, J., Chang, H., Zhang, M., Guo, X., 2018. Mid-Miocene climatic optimum: clay mineral evidence from the red clay succession, Longzhong Basin, Northern China. Palaeogeography, Palaeoclimatology, Palaeoecology 512, 46–55.
Song, B., Zhang, K., Hou, Y., Ji, J., Wang, J., Yang, Y., Yang, T., Wang, C., Shen, T., 2019. New insights into the provenance of Cenozoic strata in the Qaidam Basin, northern Tibet: constraints from combined U-Pb dating of detrital zircons in recent and ancient fluvial sediments. Palaeogeography, Palaeoclimatology, Palaeoecology 533, 109254. https://doi.org/10.1016/j.palaeo.2019.109254.
Song, S., Huang, L., Zhang, Y., Zhang, Q., Zhou, F., Liu, C., Chen, Y., Wu, Y., Zhang, Y., 2022. Middle Miocene climate transition in the Tibetan Plateau: identification and significance. Geological Magazine 159, 153–172.
Sun, Z., Yang, Z., Pei, J., Ge, X., Wang, X., Yang, T., Li, W., Yuan, S., 2005. Magnetostratigraphy of Paleogene sediments from northern Qaidam Basin, China:

implications for tectonic uplift and block rotation in northern Tibetan Plateau. Earth and Planetaty Science Letters 237, 635–646.
Tapponnier, P., Zhiqin, X., Roger, F., Meyer, B., Arnaud, N., Wittlinger, G., Jingsui, Y., 2001. Oblique stepwise rise and growth of the Tibet Plateau. Science 294, 1671. https://doi.org/10.1126/science.105978.
Tateo, F., 2020. Clay minerals at the Paleocene–Eocene thermal maximum: interpretations, limits, and perspectives. Minerals 10, 1073. https://doi.org/10.3390/min10121073.
Taylor, S.R., McLennan, S.M., 1985. The Continental Crust: Its Composition and Evolution. Blackwell Scientific Publication, Oxford, p. 312.
Thiry, M., 2000. Palaeoclimatic interpretation of clay minerals in marine deposits: an outlook from the continental origin. Earth-Science Reviews 49, 201–221.
Ulmann, M., Wildi, W., Lemmin, U., 2003. Sediment distribution on a current-dominated lake delta (Versoix delta, Lake Geneva, Switzerland). In: Beres, M., Scheidhauer, M., Marillier, F. (Eds.), Lake Systems From the Ice Age to Industrial Time. Birkhäuser Basel, Basel, pp. 91–97.
Velde, B., 1992. Introduction to Clay Minerals: Chemistry, Origins, Uses and Environmental Significance. Chapman & Hall, London (198 pp.).
Wang, E., Xu, F., Zhou, J., Wan, J., Burchfiel, B.C., 2006. Eastward migration of the Qaidam basin and its implications for Cenozoic evolution of the Altyn Tagh fault and associated river systems. Geological Society of America Bulletin 118, 349–365.
Wang, L., Jian, X., Yang, S., Guan, P., 2012. An integrated evaluation of well L101 in Xiaoliangshan area, northwestern Qaidam Basin. Internal Report of Qinghai Oilfield Company. PetroChina (151 pp., in Chinese).
Wang, C., Hong, H., Li, Z., Liang, G., Xie, J., Song, B., Song, E., Zhang, K., 2013a. Climatic and tectonic evolution in the North Qaidam since the Cenozoic: evidence from sedimentology and mineralogy. Journal of Earth Science 24, 314–327.
Wang, C., Hong, H., Li, Z., Yin, K., Xie, J., Liang, G., Song, B., Song, E., Zhang, K., 2013b. The Eocene–Oligocene climate transition in the Tarim Basin, Northwest China: evidence from clay mineralogy. Applied Clay Science 74, 10–19.
Wang, W., Zheng, W., Zhang, P., Li, Q., Kirby, E., Yuan, D., Zheng, D., Liu, C., Wang, Z., Zhang, H., Pang, J., 2017. Expansion of the Tibetan Plateau during the Neogene. Nature Communications 8, 15887. https://doi.org/10.1038/ncomms15887.
Wang, Z., Huang, C., Licht, A., Zhang, R., Kemp, D.B., 2019. Middle to Late Miocene eccentricity forcing on lake expansion in NE Tibet. Geophysical Research Letters 46, 6926–6935.
Wang, Q., Song, Y., Li, Y., 2020. Clay mineralogy of the upper Miocene-Pliocene red clay from the central Chinese Loess Plateau and its paleoclimate implications. Quaternary International 552, 148–154.
Warr, L.N., 2022. Earth's clay mineral inventory and its climate interaction: a quantitative assessment. Earth-Science Reviews 234, 104198. https://doi.org/10.1016/j.earscirev.2022.104198.
Wu, W., Xu, S., Yang, J., Yin, H., Lu, H., Zhang, K., 2010. Isotopic characteristics of river sediments on the Tibetan Plateau. Chemical Geology 269, 406–413.
Wu, F., Fang, X., An, C., Herrmann, M., Zhao, Y., Miao, Y., 2013. Over-representation of Picea pollen induced by water transport in arid regions. Quaternary International 298, 134–140.
Wu, F., Herrmann, M., Fang, X., 2014. Early Pliocene paleo-altimetry of the Zanda Basin indicated by a sporopollen record. Palaeogeography, Palaeoclimatology, Palaeoecology 412, 261–268.
Wu, T., Qin, B., Brookes, J.D., Yan, W., Ji, X., Feng, J., 2019a. Spatial distribution of sediment nitrogen and phosphorus in Lake Taihu from a hydrodynamics-induced transport perspective. Science of the Total Environment 650, 1554–1565.
Wu, M., Zhuang, G., Hou, M., Miao, Y., 2019b. Ecologic shift and aridification in the northern Tibetan Plateau revealed by leaf wax n-alkane δ^2H and $\delta^{13}C$ records. Palaeogeography, Palaeoclimatology, Palaeoecology 514, 464–473.
Wu, C., Zuza, A.V., Chen, X.H., Ding, L., Levy, D.A., Liu, C.F., Liu, W.C., Jiang, T., Stockli, D.F., 2019c. Tectonics of the eastern Kunlun Range: cenozoic reactivation of a Paleozoic-Early Mesozoic Orogen. Tectonics 38, 1609–1650.
Wu, M., Zhuang, G., Hou, M., Liu, Z., 2021. Expanded lacustrine sedimentation in the Qaidam Basin on the northern Tibetan Plateau: manifestation of climatic wetting during the Oligocene icehouse. Earth and Planetary Science Letters 565, 116935. https://doi.org/10.1016/j.epsl.2021.116935.
Xia, G., Wu, C., Li, G., Li, G., Yi, H., Wagreich, M., 2021. Cenozoic growth of the Eastern Kunlun Range (northern Tibetan Plateau): evidence from sedimentary records in the southwest Qaidam Basin. International Geology Review 63, 769–786.
Xiao, W., Windley, B.F., Yong, Y., Yan, Z., Yuan, C., Liu, C., Li, J., 2009. Early Paleozoic to Devonian multiple-accretionary model for the Qilian Shan, NW China. Journal of Asian Earth Sciences 35, 323–333.
Yang, R., Yang, Y., Fang, X., Ruan, X., Galy, A., Ye, C., Meng, Q., Han, W., 2019. Late Miocene intensified tectonic uplift and climatic aridification on the northeastern Tibetan Plateau: evidence from clay mineralogical and geochemical records in the Xining Basin. Geochemistry, Geophysics, Geosystems 20, 829–851.
Yao, X., Dai, S., Li, M., Hinnov, L., 2022. Orbital eccentricity and inclination metronomes in Middle Miocene Lacustrine mudstones of Jiuxi Basin, Tibet: closing an astrochronology time gap and calibrating global cooling events. Global and Planetary Change 215, 103896. https://doi.org/10.1016/j.gloplacha.2022.103896.
Yin, A., Rumelhart, P.E., Butler, R., Cowgill, E., Harrison, T.M., Foster, D.A., Ingersoll, R.V., Qing, Z., Xian-Qiang, Z., Xiao-Feng, W., Hanson, A., Raza, A., 2002. Tectonic history of the Altyn Tagh fault system in northern Tibet inferred from Cenozoic sedimentation. Geological Society of America Bulletin 114, 1257–1295.
Yin, A., Dang, Y.-Q., Zhang, M., Chen, X.-H., McRivette, M.W., 2008. Cenozoic tectonic evolution of the Qaidam basin and its surrounding regions (part 3): structural geology, sedimentation, and regional tectonic reconstruction. Geological Society of America Bulletin 120, 847–876.
Yin, J., Zhang, S., Lu, X., Wu, Z., Guo, H., Ju, Y., 2019. Controls of the Altyn Tagh Fault on the Early–Middle Miocene sedimentation in the Honggouzi Area, Qaidam Basin, western China. Journal of Asian Earth Sciences 181, 103908. https://doi.org/10.1016/j.jseaes.2019.103908.
Yu, X., Guo, Z., Du, W., Wang, Z., 2021. Coupling between surface processes and crustal deformation: insights from the late Cenozoic development of the Qaidam Basin, China. Global and Planetary Change 207, 103646. https://doi.org/10.1016/j.gloplacha.2021.103646.
Yuan, W.M., Zhang, X.T., Dong, J.Q., Tang, Y.H., Yu, F.S., Wang, S.C., 2003. A new vision of the intracontinental evolution of the eastern Kunlun Mountains, Northern Qinghai-Tibet plateau, China. Radiation Measurements 36, 357–362.
Yuan, D., Ge, W., Chen, Z., Li, C., Wang, Z., Zhang, H., Zhang, P., Zheng, D., Zheng, W., Craddock, W.H., Dayem, K.E., Duvall, A.R., Hough, B.G., Lease, R.O., Champagnac, J., Burbank, D.W., Clark, M.K., Farley, K.A., Garzione, C.N., Kirby, E., Molnar, P., Roe, G.H., 2013. The growth of northeastern Tibet and its relevance to large-scale continental geodynamics: a review of recent studies. Tectonics 32, 1358–1370.
Zachos, J.C., Dickens, G.R., Zeebe, R.E., 2008. An early Cenozoic perspective on greenhouse warming and carbon-cycle dynamics. Nature 451, 279–283.
Zhang, W., 2006. High-resolution Megnetostratigraphy of the Cenozoic Qaidam Basin, Implications for the Uplift of Tibetan Plateau. (Ph.D. thesis)LanZhou University, Lanzhou (in Chinese with English abstract).
Zhang, C., Mischke, S., 2009. A Lateglacial and Holocene lake record from the Nianbaoyeze Mountains and inferences of lake, glacier and climate evolution on the eastern Tibetan Plateau. Quaternary Science Reviews 28, 1970–1983.
Zhang, J., Zhang, Z., Xu, Z., Yang, J., Cui, J., 2001. Petrology and geochronology of eclogites from the western segment of the Altyn Tagh, northwestern China. Lithos 56, 187–206.
Zhang, H., Sun, Z., Jing, M., Lu, Y., Dong, N., Yuan, X., Cao, L., 2006. Significance of first appearance datum of cyprideis for division of Shangyoushashan and Xiayoushashan Formations in Qaidam Basin. China Petroleum Exploration 06 (104–112), 131 (in Chinese with English abstract).
Zhang, T., Song, C., Wang, Y., Zheng, H., Zhang, Z., Wu, S., Meng, Q., Fang, X., 2012. The Late Cenozoic tectonic deformation in the West Qaidam Basin and its implications. Earth Science Frontiers 19, 312–321 (in Chinese with English abstract).
Zhang, W., Fang, X., Song, C., Appel, E., Yan, M., Wang, Y., 2013. Late Neogene magnetostratigraphy in the western Qaidam Basin (NE Tibetan Plateau) and its constraints on active tectonic uplift and progressive evolution of growth strata. Tectonophysics 599, 107–116.
Zhang, C., Xiao, G., Guo, Z., Wu, H., Hao, Q., 2015. Evidence of late early Miocene aridification intensification in the Xining Basin caused by the northeastern Tibetan Plateau uplift. Global and Planetary Change 128, 31–46.
Zhang, C., Guo, Z., Deng, C., Ji, X., Wu, H., Paterson, G.A., Chang, L., Li, Q., Wu, B., Zhu, R., 2016. Clay mineralogy indicates a mildly warm and humid living environment for the Miocene hominoid from the Zhaotong Basin, Yunnan, China. Scientific Reports 6, 20012. https://doi.org/10.1038/srep20012.
Zhang, T., Fang, X., Wang, Y., Song, C., Zhang, W., Yan, M., Han, W., Zhang, D., 2018a. Late Cenozoic tectonic activity of the Altyn Tagh range: constraints from sedimentary records from the Western Qaidam Basin, NE Tibetan Plateau. Tectonophysics 737, 40–56.
Zhang, W., Jian, X., Fu, L., Feng, F., Guan, P., 2018b. Reservoir characterization and hydrocarbon accumulation in late Cenozoic lacustrine mixed carbonate-siliciclastic fine-grained deposits of the northwestern Qaidam basin, NW China. Marine and Petroleum Geology 98, 675–686.
Zhang, S., Jian, X., Pullen, A., Fu, L., Liang, H., Hong, D., Zhang, W., 2021. Tectono-magmatic events of the Qilian orogenic belt in northern Tibet: new insights from detrital zircon geochronology of river sands. International Geology Review 63, 917–940.
Zhu, W., Wu, C., Wang, J., Zhou, T., Li, J., Zhang, C., Li, L., 2017. Heavy mineral compositions and zircon U-Pb ages of Cenozoic sandstones in the SW Qaidam basin, northern Tibetan Plateau: implications for provenance and tectonic setting. Journal of Asian Earth Sciences 146, 233–250.
Zhuang, G., Hourigan, J.K., Koch, P.L., Ritts, B.D., Kent-Corson, M.L., 2011a. Isotopic constraints on intensified aridity in Central Asia around 12Ma. Earth and Planetary Science Letters 312, 152–163.
Zhuang, G., Hourigan, J.K., Ritts, B.D., Kent-Corson, M.L., 2011b. Cenozoic multiple-phase tectonic evolution of the northern Tibetan Plateau: constraints from sedimentary records from Qaidam basin, Hexi Corridor, and Subei basin, Northwest China. American Journal of Science 311, 116–152.